

Naval Research Laboratory

Washington, DC 20375-5000



AD-A248 630



NRL/MR/4440-92-6966

Secondary Instability in 3D Magnetic Reconnection

R.B. DAHLBURG

*Center for Computational Physics Development
Laboratory for Computational Physics and Fluid Dynamics*

S.K. ANTIOCHOS

*E.O. Hulburt Center for Space Research
Space Science Division*

T.A. ZANG

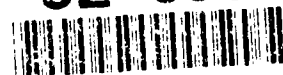
*Theoretical Flow Physics Branch
NASA Langley Research Center, Hampton, VA 23665*

April 6, 1992



02 4 17 070

92-09925



REPORT DOCUMENTATION PAGE			Form Approved OMB No 0704-0188	
Public reporting burden for this collection of information is estimated to average 1 hour per response, including the time for reviewing instructions, searching existing data sources, gathering and maintaining the data needed, and completing and reviewing the collection of information. Send comments regarding this burden estimate or any other aspect of this collection of information, including suggestions for reducing this burden, to Washington Headquarters Services, Directorate for Information Operations and Reports, 1215 Jefferson Davis Highway, Suite 1204, Arlington, VA 22202-4302, and to the Office of Management and Budget, Paperwork Reduction Project (0704-0188), Washington, DC 20503.				
1. AGENCY USE ONLY (Leave blank)	2. REPORT DATE April 6, 1992	3. REPORT TYPE AND DATES COVERED Interim		
4. TITLE AND SUBTITLE Secondary Instability in 3D Magnetic Reconnection		5. FUNDING NUMBERS		
6. AUTHOR(S) R.B. Dahlburg, S.K. Antiochos, and T.A. Zang				
7. PERFORMING ORGANIZATION NAME(S) AND ADDRESS(ES) Naval Research Laboratory Washington, DC 20375-5000		8. PERFORMING ORGANIZATION REPORT NUMBER NRL/MR/4440-92-6966		
9. SPONSORING/MONITORING AGENCY NAME(S) AND ADDRESS(ES) NASA Washington, DC 20546		10. SPONSORING/MONITORING AGENCY REPORT NUMBER		
11. SUPPLEMENTARY NOTES				
12a. DISTRIBUTION / AVAILABILITY STATEMENT Approved for public release; distribution unlimited.		12b. DISTRIBUTION CODE		
13. ABSTRACT (Maximum 200 words) We consider the transition to turbulence in three dimensional reconnection of a magnetic neutral sheet. We find that the transition can occur <i>via</i> a three-step process. First, the sheet undergoes the usual tearing instability. Second, the tearing mode saturates to form a two-dimensional quasi-steady state. Third, this secondary equilibrium is itself unstable when it is perturbed by three-dimensional disturbances. Most of this paper is devoted to the analysis and simulation of the three-dimensional linear stability properties of the two-dimensional saturated tearing layer. The numerical simulations are performed with a semi-implicit, pseudospectral-Fourier collocation algorithm. We identify a three-dimensional secondary liner stability which grows on the ideal timescale. An examination of the modal energetics reveals that the largest energy transfer is from the mean field to the three-dimensional field, with the two-dimensional field acting as a catalyst.				
14. SUBJECT TERMS Three dimensional Secondary instability Reconnection		15. NUMBER OF PAGES 47		
		16. PRICE CODE		
17. SECURITY CLASSIFICATION OF REPORT UNCLASSIFIED	18. SECURITY CLASSIFICATION OF THIS PAGE UNCLASSIFIED	19. SECURITY CLASSIFICATION OF ABSTRACT UNCLASSIFIED	20. LIMITATION OF ABSTRACT SAR	

CONTENTS

I.	INTRODUCTION	1
II.	EQUILIBRIUM AND PRIMARY INSTABILITY	5
III.	SECONDARY INSTABILITY	10
IV.	EVOLUTION OF PERTURBATIONS INTO THE FULLY NONLINEAR REGIME	17
V.	CONCLUSIONS	19
	ACKNOWLEDGEMENTS	20
	APPENDIX A - Proof of Ideal Stability for the Primary Equilibrium	20
	APPENDIX B - Numerical Algorithm	21
	REFERENCES	23

Accession For	
NTIS GRA&I	<input checked="" type="checkbox"/>
DTIC TAB	<input type="checkbox"/>
Unannounced	<input type="checkbox"/>
Justification	
By	
Distribution/	
Availability Codes	
Avail and/or	
Dist	Special
A-1	

SECONDARY INSTABILITY IN 3D MAGNETIC RECONNECTION

I. INTRODUCTION

Magnetic reconnection is believed to be responsible for a wide variety of energetic phenomena in both laboratory and astrophysical plasmas, *e.g.*, tokamak disruptions, terrestrial substorms, and solar and stellar flares. However, in astrophysical situations the magnetic Reynolds number is often so large that the well-accepted linear and non-linear reconnection processes are too slow to explain the phenomena of interest. For example, it is well known that the tearing mode growth time and the Sweet-Parker reconnection rate are too slow to account for solar flares ¹. Hence, a crucial issue for astrophysical plasmas is the determination of mechanisms that can increase the rate of tearing. Turbulence is probably the most commonly invoked process by which energy release in magnetic reconnection can be increased ^{2 3 4 5 6}.

However, the way in which a laminar reconnection process becomes turbulent has remained somewhat mysterious. This is due to several factors: Simultaneous observations of all the relevant fields at all the relevant spatial scales are presently not available for solar, space, and astrophysical plasmas. Laboratory reconnection experiments are very difficult to perform and diagnose, and theory and computation are hampered by the complexity of

the governing equations. These difficulties are not as severe for non-conducting fluids, and consequently somewhat more progress has been made on the transition problem in Navier-Stokes fluids. One very interesting finding has been that for a wide variety of simple flows an ideal secondary instability can be the first step in the transition process ^{7 8}. When the secondary instability attains a large amplitude, there is a breakdown of the laminar flow structure, generation of small scale structure, and chaotic behavior of the flow variables.

Paraphrasing Orszag and Patera ⁹ the three steps in the secondary instability process are:

- [1] a one-dimensional primary equilibrium is destabilized by a two-dimensional (2D) primary linear disturbance;
- [2] the primary linear disturbance saturates and a two-dimensional secondary equilibrium state develops; and
- [3] the two-dimensional secondary equilibrium state is destabilized by an ideal three-dimensional (3D) secondary instability.

Important flows in which such secondary instabilities occur are flat plate boundary layers ⁹, plane channel flows (Poiseuille and Couette), ^{10 9}, Hagen-Poiseuille flow ⁹, Taylor-Couette flow ¹¹ and free-shear layers ^{12 13}. It is well-known that the tearing instability in a current-sheet geometry exhibits both step [1] and step [2]. Step [1] is probably the most extensively studied problem in plasma physics, starting with the basic paper by Furth, Killeen and Rosenbluth ¹⁴. Step [2] was first demonstrated by Rutherford, ¹⁵ and has been confirmed by others ¹⁶. One of the key results of the present paper is that reconnection in a magnetic neutral sheet also exhibits Step [3]. To our knowledge, the possibility of this happening was first raised by Montgomery ¹⁷.

Why is a three-step process necessary for increasing the rate at which magnetic energy is released ? To put it another way, since going to three spatial dimensions seems to make a difference, why not just start with a fully three-dimensional primary perturbation ? This is inadequate for the following reason. The two-dimensional primary linear disturbances

grow at rates which are too slow to explain the phenomena of interest. For example, typical growth times in the solar corona are estimated to be of order tens of days, whereas solar flares are observed to occur on the time scale of minutes. In section 2 of this paper, we will show numerically that the effect of increasing three-dimensionality of the primary modes is to *decrease* their growth rate. This also can be shown analytically by proving a theorem analogous to the Squire's theorem in hydrodynamics, which states that under certain very broad conditions, two-dimensional primary perturbations will grow faster than three-dimensional primary perturbations ¹⁸. Hence, the time-scale problem exists *a fortiori* in three-dimensions, and some other process must be invoked to account for fast release of magnetic energy. In this paper we will show that what really makes a difference in timescales is the basic state, *i.e.* if instead of the standard 1D neutral sheet we use a neutral sheet plus a large dose of its 2D unstable primary eigenfunction, then ideal instabilities can be found.

The program of research described in this paper requires a reformulation of some of the usual MHD theory along more classical hydrodynamic lines, elements of which we have reported on elsewhere. The problems of stability and transition in electric current sheets are formally similar to problems in hydrodynamics ^{19 17}. For example, the hydrodynamic free-shear layer is, broadly speaking, a configuration similar to the magnetic neutral layer ¹³. This suggests that techniques developed for studying the hydrodynamic transition problem could profitably be employed in investigations of magnetic reconnection. This has been done, for example, for primary instabilities of magnetized flows ^{20 21 22}.

We have previously derived and solved a 2D magnetohydrodynamic analogue of the Orr-Sommerfeld equation ²³ for an investigation of Step [1] ²⁴. Two significant results emerged. First, it appears that, for linear resistive instability to occur, it is necessary that the electric current profile have inflection points. Steep gradients are not enough. Second, we determined the existence of a stability boundary which depends on the geometrical mean of the viscous and resistive Lundquist numbers. This has been seen by others ²⁵ ²⁶. In a subsequent investigation of Step [2], we considered the nonlinear evolution of two-

dimensional perturbed electric current sheets ²⁷. We observed the nonlinear saturation of unstable eigenmodes. The secondary equilibrium state was close to that predicted by means of a Landau stability equation. This analytical technique was first used by Stuart ²⁸ in a study of the nonlinear stability of plane Poiseuille flow and Taylor-Couette flow. When random initial conditions were used, a more complex evolution toward saturation occurred, with secondary tearing and coalescence observed ^{29 30}.

The present calculations extend the previous work to three spatial dimensions. These calculations differ from the previous ones in the boundary conditions imposed in the direction across the neutral sheet. Also, they differ in that the mean magnetic field is allowed to diffuse, *i.e.* it is not supported by an electric field. Hence the saturated state of the 2D disturbances is not really an equilibrium or a steady state. Instead, the diffusion of the mean field can be substantial. However, as will be seen, the secondary instability discussed in this paper seems to be relatively insensitive to this decay.

In the second section of this paper we set up the foundation for a discussion of the fully three-dimensional nonlinear problem. Here we first describe the governing equations, and boundary conditions. The primary equilibrium is then given, followed by a discussion of its two and three dimensional primary resistive instabilities. An Orr-Sommerfeld equation is derived and solved for the primary linear instabilities. Additional Squire equations are given for obtaining the three-dimensional primary eigenfunctions. These previous sections all lead to the third section, which is the most significant part of this paper. In this section we describe the evidence for secondary three-dimensional linear instabilities. We will present numerical evidence that this instability is ideal. We also discuss the energetics of the mode in this section. In particular, we will show that the dominant energy transfer is from the one-dimensional to the three dimensional fields. We will further show that onset of the instability can be predicted by means of a classical potential energy analysis. In the fourth section we give a preliminary description of what happens when the secondary modes attain sufficient amplitude to become nonlinear, using high-resolution, fully nonlinear 3D numerical simulations. These simulation indicate that the electric current sheet becomes

turbulent, and then “relaminarizes” due to dissipation into a new, fully three-dimensional tertiary state. We will report on these simulations more fully in a subsequent paper. The last section contains some concluding remarks.

II. EQUILIBRIUM AND PRIMARY INSTABILITY

A. The Governing Equations

We begin with the dissipative, incompressible, magnetohydrodynamic (MHD) equations, written in a dimensionless rotation form:

$$\frac{\partial \mathbf{v}}{\partial t} = \mathbf{v} \times \boldsymbol{\omega} - \nabla \Pi + M_A^2 \mathbf{j} \times \mathbf{B} + \frac{1}{R} \nabla^2 \mathbf{v}, \quad (1a)$$

$$\nabla \cdot \mathbf{v} = 0, \quad (1b)$$

$$\frac{\partial \mathbf{B}}{\partial t} = \nabla \times \mathbf{v} \times \mathbf{B} - \frac{1}{R_m} \nabla \times \nabla \times \mathbf{B}, \quad (1c)$$

and,

$$\nabla \cdot \mathbf{B} = 0, \quad (1d)$$

where $\mathbf{v}(\mathbf{x}, t) = (u, v, w) \equiv$ flow velocity, $\boldsymbol{\omega}(\mathbf{x}, t) = \nabla \times \mathbf{v} \equiv$ vorticity, $\mathbf{B}(\mathbf{x}, t) \equiv$ magnetic field, $\mathbf{j}(\mathbf{x}, t) = \nabla \times \mathbf{B} \equiv$ electric current density, $\Pi(\mathbf{x}, t) \equiv$ mechanical pressure + kinetic energy density, $R \equiv$ Reynolds number (with the viscosity assumed to be constant and uniform), $R_m \equiv$ magnetic Reynolds number (with the resistivity assumed to be constant and uniform), and $M_A \equiv$ Alfvén Mach number ($= 0$ for the pure Navier-Stokes problem). In this representation, \mathbf{B} is measured in units of the background field far from the neutral sheet. The velocities are measured in units of the Alfvén speed, $C_A = B_0 / (4\pi\rho)^{1/2}$ where the mass density, ρ , is assumed to be constant and uniform. Hence, $M_A = 1$. For a characteristic distance, L_0 , defined by the neutral sheet width, the time is measured in units of the Alfvén transit time, L_0/C_A . The regimes of applicability of such incompressible models have been discussed elsewhere^{31 32 33}.

B. Boundary Conditions

In analogy with the hydrodynamic problems, we refer to the spatial coordinate along the magnetic field (x) as the fieldwise direction, the spatial coordinate across the magnetic neutral sheet (z) as the cross-sheet direction, and the remaining spatial coordinate (y) as the sheetwise direction. We consider a system with periodic boundary conditions in the fieldwise and sheetwise directions. In the cross-sheet direction we want the magnetic field to merge into the background field as it moves away in z from the neutral sheet. Hence we want to enforce

$$B_x(\pm\infty) = \pm 1; B_y(\pm\infty) = B_z(\pm\infty) = 0. \quad (2)$$

We impose this computationally with free-slip boundary conditions ³⁴:

$$\frac{\partial B_x}{\partial z} = \frac{\partial B_y}{\partial z} = B_z = 0 \text{ at } L_3 \quad (3a)$$

and

$$\frac{\partial u}{\partial z} = \frac{\partial v}{\partial z} = w = 0 \text{ at } L_3, \quad (3b)$$

where L_3 is the computational boundary in the cross-sheet direction.

C. Primary Equilibrium

To obtain the primary instability, we assume the following linearized decomposition:

$$\mathbf{v}(x, y, z, t) = U_0(z)\hat{\mathbf{e}}_x + \mathbf{v}'(x, y, z, t), \quad (4a)$$

$$\mathbf{B}(x, y, z, t) = B_0(z)\hat{\mathbf{e}}_x + \mathbf{b}'(x, y, z, t), \quad (4b)$$

and for the pressure:

$$P(x, y, z, t) = P_0(z) + p'(x, y, z, t). \quad (4c)$$

For the primary neutral sheet equilibrium we choose

$$U_0(z) = 0, \quad (5a)$$

and,

$$B_0(z) = \tanh z. \quad (5b)$$

The pressure is determined by taking the divergence of equation 1a, and solving the resulting Poisson equation. This configuration has been studied by, among others, Schnack and Killeen³⁵.

D. Primary Two- and Three-dimensional Instabilities

After linearizing equations 1a – 1d about the equilibrium given in equations 5, we assume that the first-order terms can be decomposed in the following manner:

$$f'(x, y, z, t) = \tilde{f}(z) e^{i\alpha z + i\beta y - i\omega t}, \quad (6)$$

in which α is the fieldwise wavenumber, β is the sheetwise wavenumber, and ω is the complex growth rate. After eliminating the pressure, the primary linear perturbations we will employ are unstable eigenfunctions of the following equations, where $D \equiv d/dz$ and the tildes have been dropped:

$$\{D^2 - (\alpha^2 + \beta^2)\}^2 w - i\alpha R U_0 \{D^2 - (\alpha^2 + \beta^2)\} w + i\alpha R (D^2 U_0) w = \quad (7a)$$

$$- i\omega R \{D^2 - (\alpha^2 + \beta^2)\} w + i\alpha R M_A^2 [(D^2 B_0) b_z - B_0 \{D^2 - (\alpha^2 + \beta^2)\} b_z],$$

$$\{D^2 - (\alpha^2 + \beta^2) - i\alpha R_m U_0 + i\omega R_m\} b_z = -i\alpha R_m B_0 w, \quad (7b)$$

with the boundary conditions:

$$w \pm (\infty) = Dw(\pm\infty) = b_z(\pm\infty) = 0. \quad (7c)$$

Equations 7 are a generalization of the 3D Orr-Sommerfeld equation to include magnetic effects. Note also that we have written equation 7 in a general form which includes a mean flow.

The linear equations are solved using the Chebyshev τ technique, which was first applied to the Orr-Sommerfeld equation by Orszag³⁶ The mesh is stretched in the vertical direction with a hyperbolic mapping¹³. For the velocity free shear layer, the code reproduces the linear growth rates reported by Metcalfe *et al.*¹³ when $M_A = 0$.

It can be shown that in the limit of zero viscosity and resistivity, there are no unstable modes of equation 7. A proof of this point is given in Appendix A. When the resistivity and viscosity are finite, the unstable modes of equation 7 have an imaginary eigenvalue, real w , and imaginary b_z . Growth rates for some of these modes are provided in Table I, where a unit magnetic Prandtl (i.e. $R_m = R$) number has been assumed. All of the cases listed in Table I have $\alpha = 0.2$. Note that the system size is scaled by width of the neutral sheet, so that $\alpha = 0.2$ implies a wavelength for the perturbation of 10π times the sheet width. In Table I, the 2D primary instability growth rates are listed under γ_{2D} , and the 3D rates are listed under γ_{3D} . The last column of Table I will be discussed in the section on secondary instability. Of particular interest is the well-known decrease in the growth rate as the resistive Reynolds number increases (note that since we have set $R = R_m$, the growth rates in Table I also reflect viscous effects, i.e., a stabilization as R decreases).

Figure 1 shows some eigenfunctions for this problem to illustrate the effect of increasing the sheetwise wavenumber. In this figure, the modes are normalized to the maximum value of b_z . Figure 1a is the familiar primary 2D unstable eigenfunction, while figures 1b and 1c show unstable modes with β values of 0.2 and 0.5, respectively. The mode appears to concentrate about the neutral line with increasing β , and the ratio of the maximum of w to the maximum of b_z decreases. Figure 1d shows a purely damped mode for $\beta = 2$. We note here that the linear analysis also can be done for more physically interesting, i.e. much higher, values of the Reynolds numbers. We limit ourselves here to Reynolds numbers for which we can presently perform accurate, three-dimensional, fully nonlinear numerical

simulations.

The most important result for this paper concerns the variation of primary instability growth rates with sheetwise wavenumber. Figure 2 shows some computed unstable eigenvalues of equations 7 as a function of the sheetwise wavenumber, β . It is evident from the figure that increasing β leads to a decrease in the primary instability growth rate. Above $\beta = 0.2$, there is a linear decrease in growth rate. At high enough β a complete stabilization occurs. This can, in fact, be shown analytically by proving a Squire's theorem for the 3-D system, i.e., the three dimensional linear modes always have a lower growth rate than the 2D modes. For this reason, one might conclude that 3D modes could be safely ignored in considering the evolution of this system. The calculations presented in section 3 will invalidate this assumption.

Once the eigenfunctions have been determined from equations 7 the other components of the fields must be determined for use in initializing the nonlinear code. In two spatial dimensions this is easily done by means of the solenoidality relation for the velocity and magnetic fields. In three spatial dimensions, we must solve a perturbed vorticity (or Squire) equation:

$$\begin{aligned} \{D^2 - (\alpha^2 + \beta^2) - i\alpha R U_0\}(\beta u - \alpha v) + i\alpha M_A^2 R B_0(\beta b_z - \alpha b_y) = \\ (8a) \\ - i\omega R(\beta u - \alpha v) - \beta R[(DU_0)w - M_A^2 (DB_0)b_z]. \end{aligned}$$

and a similar equation for the perturbed electric current:

$$\begin{aligned} \{D^2 - (\alpha^2 + \beta^2) - i\alpha R_m U_0\}(\beta b_z - \alpha b_y) + i\alpha R_m B_0(\beta u - \alpha v) = \\ (8b) \\ - i\omega R_m(\beta b_z - \alpha b_y) - \beta R_m[(DU_0)b_z - (DB_0)w]. \end{aligned}$$

with the boundary conditions:

$$\beta u(\pm\infty) - \alpha v(\pm\infty) = 0 \quad (8c)$$

$$\beta b_x(\pm\infty) - \alpha b_y(\pm\infty) = 0 \quad (8d)$$

The remaining field components then can be determined by using the solenoidality relations for the velocity and magnetic field.

E. Secondary Equilibrium – Nonlinear Saturation of 2D Primary Instability

Since the 2D unstable eigenmode has the fastest growth rate, it is reasonable to suppose that it will be the first mode to develop to the point where nonlinear effects become significant. It has been determined, both analytically and numerically, that this mode saturates into a secondary equilibrium when it becomes sufficiently large. Rutherford¹⁵ in his classic analysis showed that the tearing mode changes from exponential to linear growth at a mode amplitude which varies approximately inversely with magnetic Reynolds number. Hence, the mode saturates at very low amplitude, whereupon the reconnection rate becomes that due simply to ohmic diffusion. The conclusion is that tearing in two dimensions cannot account for the rapid energy release observed in phenomena such as solar flares.

Figure 3 shows the magnetic topology, electric current, and vorticity for a system close to the saturated state. This resembles the initial state that we use for the three-dimensional perturbation. We note in Figure 3a the familiar magnetic island which characterizes the tearing mode, in Figure 3b the electric current filamentation at the magnetic X-point³⁷, and in Figure 3c the flow pattern. Typically, the kinetic energy of the 2D saturated state is much less than the magnetic energy, which demonstrates that the evolution has become dominated by diffusion.

III. SECONDARY INSTABILITY

In this chapter we provide numerical evidence for the existence of a secondary instability of the neutral sheet, investigate its parametric dependence, and show that the onset of the instability is predictable by a classical potential energy analysis. The investigation

relies on numerical simulation of Equations 1. The semi-implicit Fourier pseudospectral - Fourier collocation scheme that we employ is described in Appendix B.

A. Evidence for a secondary instability

We initialize the magnetic field in the following way:

$$\mathbf{B}(x, y, z, t = 0) = B_0(z)\hat{\mathbf{e}}_z + \epsilon_{2d}\mathbf{B}_{2d}(z)e^{i\alpha z} + \epsilon_{3d}\mathbf{B}_{3d}(z)e^{i\alpha(z+\phi)+i\beta y}, \quad (9a)$$

where ϵ_{2d} is the amplitude of the two-dimensional MHD Orr-Sommerfeld eigenmode (\mathbf{B}_{2d}), ϵ_{3d} is the amplitude of the three-dimensional MHD Orr-Sommerfeld eigenmode (\mathbf{B}_{3d}), and ϕ is the phase shift between the 2D and the 3D mode (set to $\pi/2$ throughout). For the velocity field we have:

$$\mathbf{v}(x, y, z, t = 0) = \epsilon_{2d}\mathbf{v}_{2d}(z)e^{i\alpha z} + \epsilon_{3d}\mathbf{v}_{3d}(z)e^{i\alpha(z+\phi)+i\beta y}. \quad (9b)$$

The magnetic field eigenfunctions are normalized so that $\max_z |B_z(z)| = 1$, and the velocity eigenfunctions are scaled proportionately (see Figure 1).

We now demonstrate that the nonlinearly saturated two-dimensional tearing layer is subject to three-dimensional, secondary instabilities. To do this we first prepare an initial state consisting of the tearing layer plus a large dose of the 2D primary unstable eigenfunction ($\epsilon_{2d} = .02$), so that the system is close to the 2D nonlinearly saturated state. Previous research has shown that the form of the perturbation is relatively unchanged in the saturated state, *i.e.*, the “shape assumption” holds^{27 28}. We then perturb this state with a much smaller dose of the appropriate 3D primary unstable eigenfunction ($\epsilon_{3d} = 1 \times 10^{-8}$). These initial conditions represent a state that is highly probable, since the primary 2D modes outstrip the 3D primary modes and saturate first, creating a kind of secondary equilibrium in which the 3D disturbances subsequently evolve.

One respect in which our simulation might differ from others is that we do not hinder the evolution of the current layer, but instead allow it to dissipate freely. We can quantify

the spreading of the current layer by defining a mean current thickness as:

$$\ell_c = B_{ext} \left[\frac{1}{V} \left\langle \frac{\partial B_z}{\partial z} \right\rangle \right]_{maz}^{-1}, \quad (10)$$

where V equals the system volume, and B_{ext} denotes the magnetic field exterior to the tearing layer, i.e., 1. Furthermore, the bracket notation is used to denote volume integrals: $\langle f \rangle = \int_0^{2\pi/\alpha} \int_0^{2\pi/\beta} \int_{-z_0}^{z_0} f \, dx \, dy \, dz$. Initially, $\ell_c = 1$ by definition. For case 9 (see Table I) with $R_m = 200$, at $t = 200$, $\ell_c = 3.10$. At the same time, for case 18 with $R_m = 1000$, $\ell_c = 1.48$. Hence the spreading of the current layer due to dissipation is significant. However, as we will show, the evolution of the secondary mode appears to be relatively insensitive to this spreading.

Although we initialize the fields with one mode in x , after a few Alfvén times when the system is near the saturated state, more than one mode will be excited. Hence, it is more accurate to represent the fields as having the form of a 2D tearing layer perturbed by a 3D disturbance:

$$\mathbf{B} = B^{(1)}(z, t) \hat{\mathbf{e}}_x + \sum_{|m| < M/2} \tilde{\mathbf{B}}_{m0}^{(2)}(z, t) e^{i\alpha m x} + \sum_{n=\pm 1} \sum_{|m| < M/2} \tilde{\mathbf{B}}_{mn}^{(3)}(z, t) e^{i\alpha m x} e^{i\beta n y}, \quad (11a)$$

and

$$\mathbf{v} = U^{(1)}(z, t) \hat{\mathbf{e}}_x + \sum_{|m| < M/2} \tilde{\mathbf{v}}_{m0}^{(2)}(z, t) e^{i\alpha m x} + \sum_{n=\pm 1} \sum_{|m| < M/2} \tilde{\mathbf{v}}_{mn}^{(3)}(z, t) e^{i\alpha m x} e^{i\beta n y}, \quad (11b)$$

where the tilde denotes the Fourier coefficient.

To track the evolution of the 3D secondary modes, we define a 3D total energy given by

$$E_{3D} = \frac{1}{2} \int (|\mathbf{B}^{(3)}|^2 + |\mathbf{v}^{(3)}|^2) d^3x. \quad (12a)$$

This, as well as the 2D energy, given by:

$$E_{2D} = \frac{1}{2} \int (|\mathbf{B}^{(2)}|^2 + |\mathbf{v}^{(2)}|^2) d^3x, \quad (12b)$$

is shown in figure 4, for case 9 of Table I. After about fifty Alfvén times E_{2D} flattens out and a linear phase is evident in E_{3D} . As previously noted, the growth of the 3D energy is relatively independent of the dissipative spreading of the neutral sheet. Results of several of these runs, with different values of β and the Reynolds numbers, are shown in Table I. In this table we give the total 3D energy average growth rates for the secondary instability, γ , where

$$\frac{1}{2E_{3D}} \frac{dE_{3D}}{dt} = \gamma, \quad (13)$$

and $200 \leq t \leq 250$. For case 9, for example, the secondary mode grows at more than double the rate of the primary 3D mode. All of the runs listed in Table I were performed with $\alpha = 0.2$. Limited tests of α variation for case 3 in the table indicated a falloff in γ for higher and lower α than 0.2. We did not investigate further this rather fortuitous result.

Several conclusions can be drawn from the information presented in Table I: (a.) There is an increase in the secondary mode growth rate at low Reynolds number, then a relative independence at higher Reynolds numbers; (b.) There is an instability threshold in the Reynolds number, i.e., the secondary mode can be stabilized if there is enough diffusion. This might explain why this mode is not observed in the reported collisionless tearing experiments, which have had magnetic Reynolds numbers of 10 to 20^{38 39}, and (c.) There is a high β cutoff of the secondary instability. The cutoff value in β increases as the Reynolds numbers increase and is given approximately by $\beta_c \approx .25R_m^{1/2}$. However, this estimate is clouded somewhat by our use of a unit magnetic Prandtl number. Furthermore, it is of interest that linearly stable 3D primary eigenmodes can trigger 3D secondary instabilities. Unfortunately, we are somewhat limited in the magnitude of Reynolds numbers that we can simulate accurately with direct numerical simulation. However, we note that even at

these modest values, the growth rates for the secondary instability can exceed the resistive primary instability growth rates. In addition, these latter rates should decrease as the magnetic Reynolds number is increased.

B. Energetics of the secondary instability

While the behavior of γ is indicative of a secondary linear instability, it provides little insight into the dynamics of the unstable mode. In particular, we would like more information on the interactions between the 1D, 2D, and 3D fields. To obtain this information we generalize the hydrodynamic analysis of Orszag and Patera (1983) to the MHD case.

Hence, we now decompose the magnetic and velocity fields so that the various fields are mutually orthogonal (time dependence of the fields is assumed): The one dimensional fields are given by:

$$\mathbf{B}^{[1]}(z) = (B^{(1)}(z) + B_{00}^{(2)}(z))\hat{\mathbf{e}}_z, \quad (14a)$$

and

$$\mathbf{v}^{[1]}(z) = (U^{(1)}(z) + v_{00}^{(2)}(z))\hat{\mathbf{e}}_z = 0 + 0 = 0 \quad (14b).$$

For the two-dimensional fields we have:

$$\mathbf{B}^{[2]}(x, z) = \mathbf{B}^{(2)}(x, z) - B_{00}^{(2)}(z)\hat{\mathbf{e}}_z, \quad (14c)$$

$$\mathbf{v}^{[2]}(x, z) = \mathbf{v}^{(2)}(x, z) - v_{00}^{(2)}(z)\hat{\mathbf{e}}_z. \quad (14d)$$

The three-dimensional fields are given by:

$$\mathbf{B}^{[3]}(x, y, z) = \mathbf{B}^{(3)}(x, y, z), \quad (14e)$$

$$\mathbf{v}^{[3]}(x, y, z) = \mathbf{v}^{(3)}(x, y, z). \quad (14f)$$

The total energies (magnetic plus kinetic) corresponding to these fields evolve as:

$$\frac{dE_1}{dt} = -T_{12} - T_{13} + D_1, \quad (15a)$$

$$\frac{dE_2}{dt} = T_{12} - T_{23} + D_2, \quad (15b)$$

$$\frac{dE_3}{dt} = T_{13} + T_{23} + D_3. \quad (15c)$$

Our interest is in the last equation, where E_3 represents the energy in the 3D fields, T_{13} represents the interaction of the 1D and 3D fields, T_{23} represents the interaction of the 2D and 3D fields, and D_3 represents the ohmic and viscous diffusion of the 3D field. Interpretation of the other terms follows from this.

It is straightforward to evaluate T_{13} from the equation 15a, viz.,

$$T_{13} = - \int \mathbf{B}^{[1]} \cdot (\nabla \times \mathbf{v}^{[3]} \times \mathbf{B}^{[3]}) d^3x. \quad (16)$$

T_{23} is then given by:

$$T_{23} = \int \mathbf{v}^{[3]} \cdot (\mathbf{v} \times \boldsymbol{\omega}) d^3x + \int \mathbf{v}^{[3]} \cdot (\nabla \times \mathbf{B} \times \mathbf{B}) d^3x + \int \mathbf{B}^{[3]} \cdot (\mathbf{v} \times \mathbf{B}) d^3x - T_{13}, \quad (17)$$

and D_3 is given by:

$$D_3 = \frac{1}{R_m} \int |\nabla \times \mathbf{B}^{[3]}|^2 d^3x + \frac{1}{R} \int |\nabla \times \mathbf{v}^{[3]}|^2 d^3x. \quad (18)$$

To obtain a rate for energy transfer to and from the 3D mode, we compute

$$\bar{\gamma} = \frac{T_{13}}{2E_3} + \frac{T_{23}}{2E_3} + \frac{D_3}{2E_3} = \bar{T}_{13} + \bar{T}_{23} + \bar{D}_3, \quad (19)$$

where $E_3 = \int (|\mathbf{B}^{[3]}|^2 + |\mathbf{v}^{[3]}|^2) d^3x$. To check the accuracy of this decomposition we compare $\bar{\gamma}$ with γ .

Figure 5 shows \bar{T}_{13} , \bar{T}_{23} , \bar{D}_3 and $\bar{\gamma}$ as functions of time for case 9 of Table I. It is apparent that the total growth rate is almost entirely due to the interaction between the 1D and 3D fields. The 2D field extracts energy from the 3D field during the secondary linear phase. The dissipation of course provides an energy sink throughout the run. Figure 6 shows the same quantities for case 11, to show how the secondary mode transfer terms vary with β . This case is near to the maximum growth rate observed in β , all other parameters being the same (see Table I). An increase in \bar{T}_{13} is seen, but this is almost balanced by a decrease in \bar{T}_{23} . Figure 7 shows the same quantities for case 13, which is nearly stable. It can be seen that increases in β lead to increased dissipation through decreased \bar{D}_3 , whereas the transfer term \bar{T}_{13} does not change very much. Finally, Figure 8 shows the same quantities for case 16, to illustrate the effect of increasing the Reynolds numbers. Comparing this to figure 5, we see that \bar{T}_{13} remains about the same, \bar{D}_3 increases, and \bar{T}_{23} decreases. However, the secondary mode growth rate remains about the same.

C. Potential Energy Analysis

As previously noted, the primary equilibrium is stable to ideal perturbations (we prove this point in Appendix A). On the other hand, we have also seen evidence that the secondary instability is ideal. The secondary instability growth rates listed in Table I appear to be relatively insensitive to changes in the Reynolds numbers. Detailed analysis of energy transfer shows that the 1D to 3D transfer also is relatively unchanged by variation of Reynolds numbers (compare figure 5 and 8). These observations suggest that the stability of the secondary mode might be predictable by means of a classical energy analysis for ideal instability⁴⁰.

Since the kinetic energy of the secondary equilibrium is much less than the magnetic energy, we assume that the secondary equilibrium state is static, i.e.,

$$\mathbf{v}^{\{1\}} = 0, \quad (20a)$$

and

$$\mathbf{B}^{\{1\}} = B^{[1]}(z)\tilde{\mathbf{e}}_z + \mathbf{B}^{[2]}(x, z). \quad (20b)$$

We can then calculate the potential energy δW relevant to our system

$$\delta W = \frac{1}{4\pi} \int \{ |\nabla \times [\mathbf{v}^{[3]} \times \mathbf{B}^{(1)}]|^2 - [\mathbf{v}^{[3]} \times (\nabla \times \mathbf{B}^{(1)})] \cdot (\nabla \times [\mathbf{v}^{[3]} \times \mathbf{B}^{(1)}]) \} d^3x. \quad (21)$$

Note that the surface terms drop out due to our boundary conditions. If δW is less than zero, the system is unstable. Figure 10 shows the same data as in figure 4, along with the sign of δW as a function of time for case 9 of Table I. Note that δW remains positive approximately until the 2D mode has saturated. It then becomes negative at about the time that the 3D mode takes off. This provides additional evidence that the secondary instability is ideal, i.e., independent of the Reynolds numbers.

IV. EVOLUTION OF PERTURBATIONS INTO THE FULLY NONLINEAR REGIME

One important remaining question is what happens when the secondary modes become nonlinear ? Is there a transition to turbulence, or does the mode saturate into a tertiary equilibrium ? Here we briefly describe some high resolution runs which suggest that the answer is both, i.e. there is a burst of turbulence followed by a relaminarization due to the relatively high dissipation employed in the simulation. The runs are initialized with eigenfunctions which evolve into the nonlinear regime, with $\alpha = 0.2, \beta = 0.2, R = R_m = 50, 100$, and $200, \epsilon_{2d} = 0.01$ and $\epsilon_{3d} = 0.001$. The resolution for these runs is $(32 \times 32 \times 64)$ modes. Some data for these runs are given in Table II.

Evidence for a burst of turbulence is provided by an examination of the enstrophy for cases 1-3 in Table II. The kinetic energy decay rate is proportional to the enstrophy, $\Omega = \langle |\omega|^2 \rangle$, i.e.,

$$\frac{dE_v}{dt} = -\frac{1}{R} \langle |\omega|^2 \rangle \quad (22)$$

and it can be used as a proxy for monitoring the level of small scale excitation. This quantity is shown for three runs at different Reynolds numbers in figure 10. For all of the cases there is a big jump in Ω around $t = 100$, followed by a slow decrease. The magnitude

of the burst increases with the Reynolds numbers, as does the subsequent level. Similar behavior is seen in the perturbed mean square electric current.

The evolution is clarified by the time histories of the perturbed components (note the normalization). Figure 11 and 12 show the logarithm of selected modal kinetic and magnetic energies, with the z direction integrated out, for case 2 in Table II. Shown are the 2D primary mode, $k_x = 0.2, k_y = 0$, the 3D primary mode $k_x = 0.2, k_y = 0.2$, and the longest wavelength sheetwise mode $k_x = 0, k_y = 0.2$. Both the magnetic and velocity fields evolve in essentially the same way. Rapid initial growth followed by saturation is seen in the sheetwise mode. The 2D and 3D primary modes exhibit a burst of growth around $t = 100$, followed by a long term secular decay. The crucial feature in Figures 11 and 12 is the rapid growth and persistence of the sheetwise mode, especially in the kinetic energy. These modes (i.e., all those with $k_x = 0$) eventually dominate the system energetics. Hence we see a burst of excitation around $t = 100$, followed by dominance of the purely sheetwise mode. The same behavior is seen in higher harmonics. Preliminary calculations at higher Reynolds numbers indicate that the non-sheetwise modes do not decay as quickly. Consequently, we conjecture that the relaminarization is a dissipative effect which will be less dominant at higher Reynolds numbers. We will address this more fully in a subsequent paper.

Some morphological features of the evolution of the secondary instability are more easily shown in configuration space. Figures 13 through 17 show, in the $(x, y, z = 0)$ plane, the time evolution of contours of $|\mathbf{B}|^2$ for run 1 in Table II. Two periods in x are shown. Figure 13 shows these contours at $t = 44$, slightly before the rapid development seen in figure 10. In this figure, the leftmost group of contours shows the position of a magnetic O-point, the next set a magnetic X-point, and so forth. A sort of kinking is evident in y , with the O-points somewhat more susceptible than the X-points. This is the basic form of the secondary mode. Figure 14 shows the increasingly nonlinear character of the disturbance. Figure 15 shows the X- and O-points beginning to interact. Figures 14 and 15 exhibit the continuing formation of more and more structure in the sheetwise

direction. Figures 16 and 17 show later stages in the evolution of the system. It of particular interest that the field gradients evolve toward being in the sheetwise direction, whereas initially they were in the fieldwise direction. Implicit in this development is the breakdown of the familiar laminar structures associated with magnetic reconnection, *e.g.*, the magnetic islands, electric current filaments, and the flow pattern shown in Figure 3. Little topological change is seen once the contours of $|\mathbf{B}|^2$ adopt the pattern shown in Figure 17.

It is important to note that we have not allowed for the development of subharmonic modes, *i.e.*, the perturbations have set the spatial scales in the fieldwise and sheetwise directions. In random noise initiated calculations that we have performed, we have identified two modes, similar to modes identified for velocity free shear layers⁴¹. (i.) a translational mode, seen in figure 13, and (ii.) a pairing mode, which occurs when subharmonic interactions are possible. This last mode is the 3D analog of the coalescence mode, and it resembles the one identified in low Reynolds number experiments^{38 39}. The presence of these two modes indicates that, as in hydrodynamical problems, the route by which a system transitions to turbulence is not unique, and it depends heavily on initial conditions.

V. CONCLUSIONS

The key result of our simulations is that the saturated 2D reconnection state is unstable to 3D perturbations. This secondary instability is non-dissipative in character, and in general it grows at a rate which exceeds the reconnection rate. The secondary mode growth rate is relatively independent of the dissipative spreading of the neutral sheet, at least on the time scales over which our simulations were performed. When the secondary mode becomes nonlinear, the system undergoes a turbulent transition to a three-dimensional quasi-steady state. During the late nonlinear phase, the sheetwise modes in the magnetic field and the velocity field eventually dominate the system.

Hence, it is legitimate to inquire into the validity of the standard reconnection scenarios. Our work suggests that the conventional current sheet, vortex quadrupole system

is difficult to sustain when the third spatial dimension is taken into account. Therefore, a steady state involving such a configuration is unlikely. The observations can be construed as supporting this contention, since the 2D laminar model consistently underestimates the energy release rates required to account for phenomena such as solar flares. Of course, we should emphasize that so far we have investigated only neutral sheets. The addition of a strong field component in the sheetwise direction might affect the evolution of an electric current sheet. We are presently addressing this issue.

ACKNOWLEDGEMENTS

We thank J. T. Karpen and J. P. Dahlburg for their suggestions on improving the manuscript. The numerical calculations reported here were performed on the NASA Ames Research Center Cray Y-MP supercomputer. This work was supported by the NASA Space Physics Theory Program, the NASA SMM Guest Investigator Program, and the Office of Naval Research.

Appendix A: Proof of Ideal Stability for the Primary Equilibrium

Consider the ideal limit of equations 7, i.e., let $R \rightarrow \infty$ and $R_m \rightarrow \infty$. Furthermore, decompose the eigenvalue as $\omega = \alpha c$. Then equations 7 become

$$0 = -c\{D^2 - (\alpha^2 + \beta^2)\}w + \{(D^2 B_0) - B_0[D^2 - (\alpha^2 + \beta^2)]\}b_z, \quad (A1a)$$

and

$$cb_z = -B_0 w, \quad (A1b)$$

where we have set $M_A = 1$ and $U_0 = 0$. We solve equation (A1b) for b_z , and substitute the result in equation (A1a). After some algebra, this reduces to the form

$$D[(c^2 - B_0^2)Dw] - (\alpha^2 + \beta^2)(c^2 - B_0^2)w = 0. \quad (A2)$$

Now multiply this equation by the complex conjugate of w , w^* , and integrate the result in the crossfield direction using free slip boundary conditions. After some manipulation, we have the result:

$$\int_{-\infty}^{+\infty} (c^2 - B_0^2)[|Dw|^2 + (\alpha^2 + \beta^2)|w|^2]dz = 0. \quad (A3)$$

Finally, separate equation (A3) into its real and imaginary parts.

$$\int_{-\infty}^{+\infty} (c_r^2 - c_i^2 - B_0^2) [|Dw|^2 + (\alpha^2 + \beta^2) |w|^2] dz = 0, \quad (\text{A4a})$$

$$c_r c_i \int_{-\infty}^{+\infty} [|Dw|^2 + (\alpha^2 + \beta^2) |w|^2] dz = 0, \quad (\text{A4b})$$

where $c_r + ic_i = c$. Here equation (A4a) is the real part of equation (A3), and equation (A4b) is the imaginary part. For equation (A4b) to be true, one of the following must be true; $c_r = 0$, $c_i = 0$, or $w(z) = 0$. We are not interested in the final option, hence one of the first two must be true. An inspection of equation (A4a) shows that the equality cannot be true if $c_r = 0$, and hence we conclude that

$$c_i = 0, \quad (\text{A5})$$

Since $\omega = \alpha c = \alpha(c_r + ic_i)$, and the primary instabilities vary in time as $e^{-i\omega t}$, the primary equilibrium is stable in the ideal limit.

Appendix B: Numerical Algorithm

We solve equations 1 together with the boundary conditions with a semi-implicit spectral scheme. The equations are discretized in the two periodic directions, x and y , with a Fourier pseudospectral scheme. In the cross-sheet direction, z , a Fourier collocation scheme is employed together with a hyperbolic mesh stretching. The method extends the algorithm of Cain *et al.* ⁴², with sine and cosine functions used in z , together with a cotangent mapping for expansion on an infinite interval (see Canuto *et al.* ⁴³, pp 74-75). The nonlinear terms are advanced in time with a third order Runge-Kutta method, while the vertical diffusion is advanced with a Crank-Nicolson scheme. A backward Euler pressure correction is performed at each time level. The same type of correction is performed at each level to ensure the solenoidality of the magnetic field ^{44 45}, i.e. we define a scalar function ϕ such that

$$\nabla^2 \phi + \nabla \cdot \mathbf{B} = 0. \quad (\text{B1})$$

The magnetic field is corrected after the advection-diffusion step so that

$$\mathbf{B}' = \mathbf{B} + \nabla\phi, \tag{B2}$$

and hence

$$\nabla \cdot \mathbf{B}' = 0. \tag{B3}$$

References

1. E. R. Priest, in *Solar Flare Magnetohydrodynamics*, ed E. R. Priest, (Gordon and Breach: New York, 1981), p 139.
2. H. R. Strauss, *Phys. Fluids* **29**, 3668 (1986).
3. H. R. Strauss, *Astrophys. J.* **326**, 412 (1988).
4. D. Biskamp and H. Welter, *Phys. Fluids B* **1**, 1964 (1989).
5. W. H. Matthaeus and S. L. Lamkin, *Phys. Fluids* **29**, 2513 (1986).
6. D. Deeds and G. Van Hoven, *J. Plasma Phys.* **42**, 269 (1989).
7. Bayly, B. J., Orszag, S. A., and Herbert, Th., *Ann. Rev. Fluid Mech.* **20**, 359 (1988).
8. Herbert, Th., *Ann. Rev. Fluid Mech.* **20**, 487 (1988).
9. Orszag, S. A., and Patera, A. T., *J. Fluid Mech.* **128**, 347 (1983).
10. Orszag, S. A., and Kells, L. C., *J. Fluid Mech.* **96**, 159 (1980).
11. Davey, A., DiPrima, R. C., and Stuart, J. T., *J. Fluid Mech.* **31**, 17 (1968).
12. Kelly, R. E., *J. Fluid Mech.* **27**, 657 (1967).
13. R. W. Metcalfe, S. A. Orszag, M. E. Brachet, S. Menon, and J. J. Riley, *J. Fluid Mech.* **184**, 207 (1987).
14. Furth, H, Killeen, J. and Rosenbluth, M. N., *Phys. Fluids* **6**, 459 (1963).
15. Rutherford, P. H., *Phys. Fluids* **16**, 19003 (1973).
16. White, R. B., Monticello, D. A., Rosenbluth, M. N., and Waddell, B. V., *Phys. Fluids* **20**, 800 (1977).
17. D. Montgomery, in *Spectral Methods for Partial Differential Equations*, eds R. G. Voight, D. Gottlieb, and M.Y. Hussaini (Siam, Philadelphia, 1984).
18. H. B. Squire, *Proc. Roy. Soc. A* **142**, 621 (1933).

19. D. Montgomery, *Physica Scripta* **T2:2**, 506 (1982).
20. J. T. Stuart, *Proc. Roy. Soc A* **221**, 189 (1954).
21. E. P. Velikhov, *Sov. Phys. JETP* **36**, 848 (1959).
22. P. R. Nachtsheim and E. Reshotko, *NASA Tech. Note D-3144*, (1965).
23. Drazin, P. G. and Reid, W. H., *Hydrodynamic Stability* (Cambridge, New York, 1984), p156.
24. R. B. Dahlburg, T. A. Zang, D. Montgomery, and M. Y. Hussaini, *Proc. Nat. Acad. Sci. USA* **80**, 5798 (1983).
25. A. Bondeson and J. R. Sobel, *Phys. Fluids* **27**, 2028 (1984).
26. G. Einaudi and F. Rubini, *Phys. Fluid B* **1**, 2224 (1989).
27. R. B. Dahlburg, T. A. Zang, and D. C. Montgomery, *J. Fluid Mech.* **169**, 71 (1986).
28. J. T. Stuart, *J. Fluid Mech.* **4**, 1 (1958).
29. R. D. Parker, R. L. Dewar, and J. I. Johnson, *Phys. Fluids B* **2**, 509 (1990).
30. F. Malara, P. Veltri, and V. Carbone, *Phys. Fluids B* **3**, 1801 (1991).
31. R. B. Dahlburg and J. M. Picone, *Phys. Fluids B* **1**, 2153 (1989).
32. J. M. Picone and R. B. Dahlburg, *Phys. Fluids B* **3**, 29 (1991).
33. D. C. Montgomery, in *Lecture Notes in Turbulence*, eds. J. R. Herring and J. C. McWilliams (World Scientific, Teaneck, NJ, 1989), p 75.
34. S. A. Orszag and Y. -H. Pao, in *Turbulent Diffusion in Environmental Pollution*, ed. F. N. Frenkel, and R. E. Munn, (Academic Press, New York, 1974), p 225.
35. D. Schnack and J. Killeen, *J. Comp. Phys.* **35**, 110 (1980).
36. S. A. Orszag, *J. Fluid Mech.* **50**, 689 (1971).
37. W. H. Matthaeus and D. Montgomery, *J. Plasma Phys.* **25**, 11 (1981).

38. W. Gekelman and H. Pfister, *Phys. Fluids* **31**, 2017 (1988).
39. W. Gekelman, H. Pfister, and J. R. Kan *J. Geophys. Res.* **96**, 3829 (1991).
40. I. B. Bernstein, E. A. Frieman, M. D. Kruskal, and R. M. Kulsrud, *Proc. Roy. Soc. (London)* **A 244**, 17 (1958).
41. R. T. Pierrehumbert and S. E. Widnall, *J. Fluid Mech.* **114**, 59 (1982).
42. Cain, A. B., Ferziger, J. H., and Reynolds, W. C., *J. Comp. Phys.* **56**, 272 (1984).
43. C. Canuto, M. Y. Hussaini, A. Quarteroni, and T. A. Zang, *Spectral Methods in Fluid Dynamics* (Springer-Verlag, New York, 1988).
44. J. U. Brackbill and D. C. Barnes, *J. Comp. Phys.* **35**, 426 (1980).
45. Stephens, A. B., Bell, J. B., Solomon, J. M., and Hackerman, L. B., *J. Comp. Phys.* **53**, 152 (1984).

TABLE I.

Case	$R = R_m$	β	γ_{2d}	γ_{3d}	γ
1	10	0.2	.042485	.023348	-.003
2	20	0.2	.043658	.029808	.007
3	100	0.2	.033066	.025587	.046
4	100	0.5	.033066	.007061	.055
5	100	1.0	.033066	<i>STABLE</i>	.048
6	100	1.5	.033066	<i>STABLE</i>	.031
7	100	2.0	.033066	<i>STABLE</i>	.006
8	100	2.5	.033066	<i>STABLE</i>	-.023
9	200	0.2	.026636	.020737	.051
10	200	0.5	.026636	.007288	.062
11	200	1.0	.026636	<i>STABLE</i>	.059
12	200	1.5	.026636	<i>STABLE</i>	.051
13	200	2.0	.026636	<i>STABLE</i>	.039
14	200	2.5	.026636	<i>STABLE</i>	.023
15	200	3.0	.026636	<i>STABLE</i>	.004
16	200	3.5	.026636	<i>STABLE</i>	-.017
17	400	0.2	.020551	.015915	.051
18	1000	0.2	.013818	.010528	.048

TABLE II.

Case	$\alpha = \beta$	$R = R_m$	ϵ_{2d}	ϵ_{3d}	γ_{2d}	γ_{3d}
1	0.2	50	.02	.001	.03896	.02938
2	0.2	100	.02	.001	.03307	.02559
3	0.2	200	.02	.001	.02664	.02074

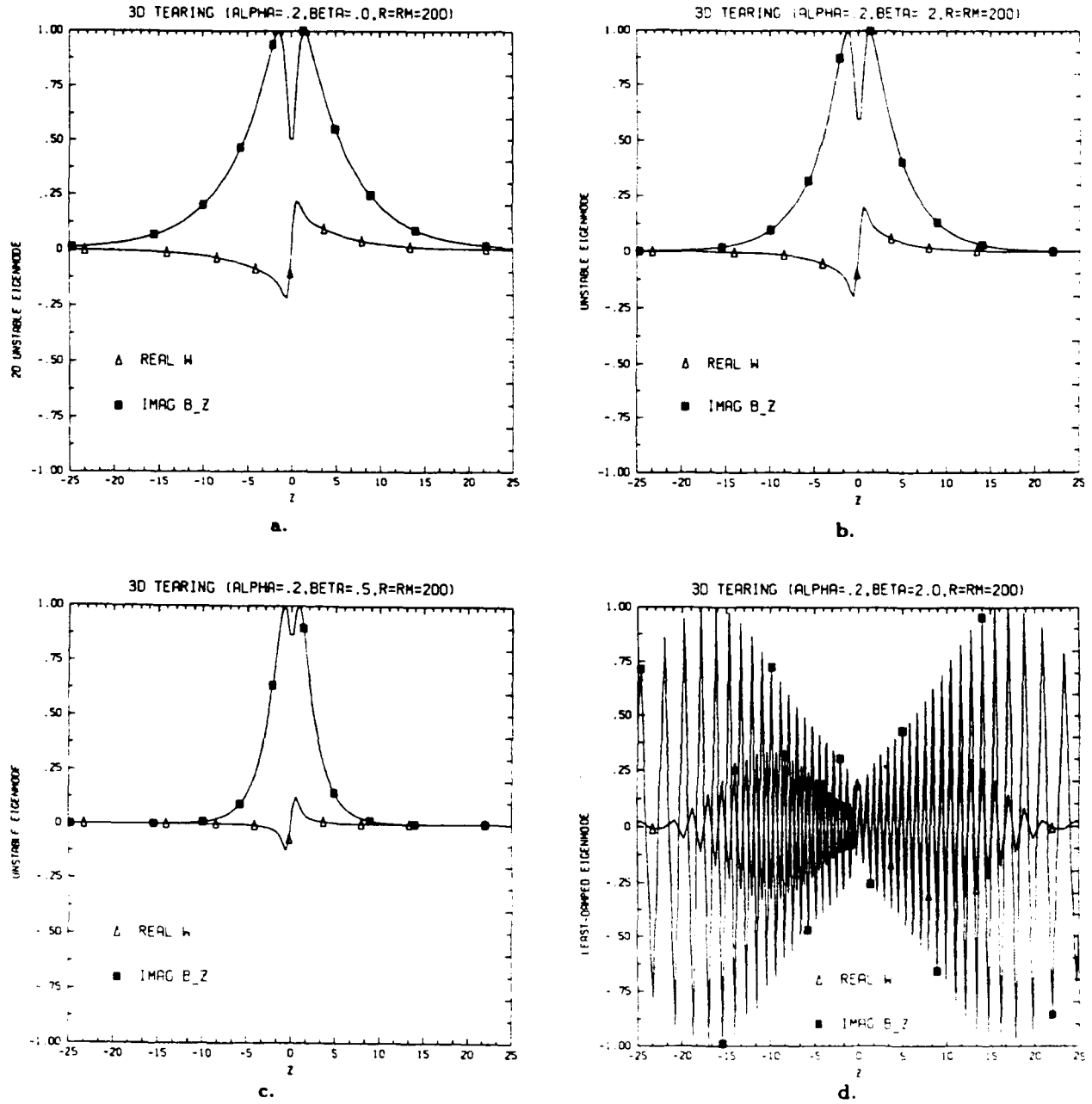


Figure 1. Primary unstable eigenmode *vs* z , the cross-sheet direction. All modes have $\alpha = .2, R = R_m = 200$. a. $\beta = 0$, 2D primary unstable mode; b. $\beta = .2$, 3D primary unstable mode; c. $\beta = .5$, 3D primary unstable mode; d. $\beta = 2.$, a nonpropagating 3D damped mode.

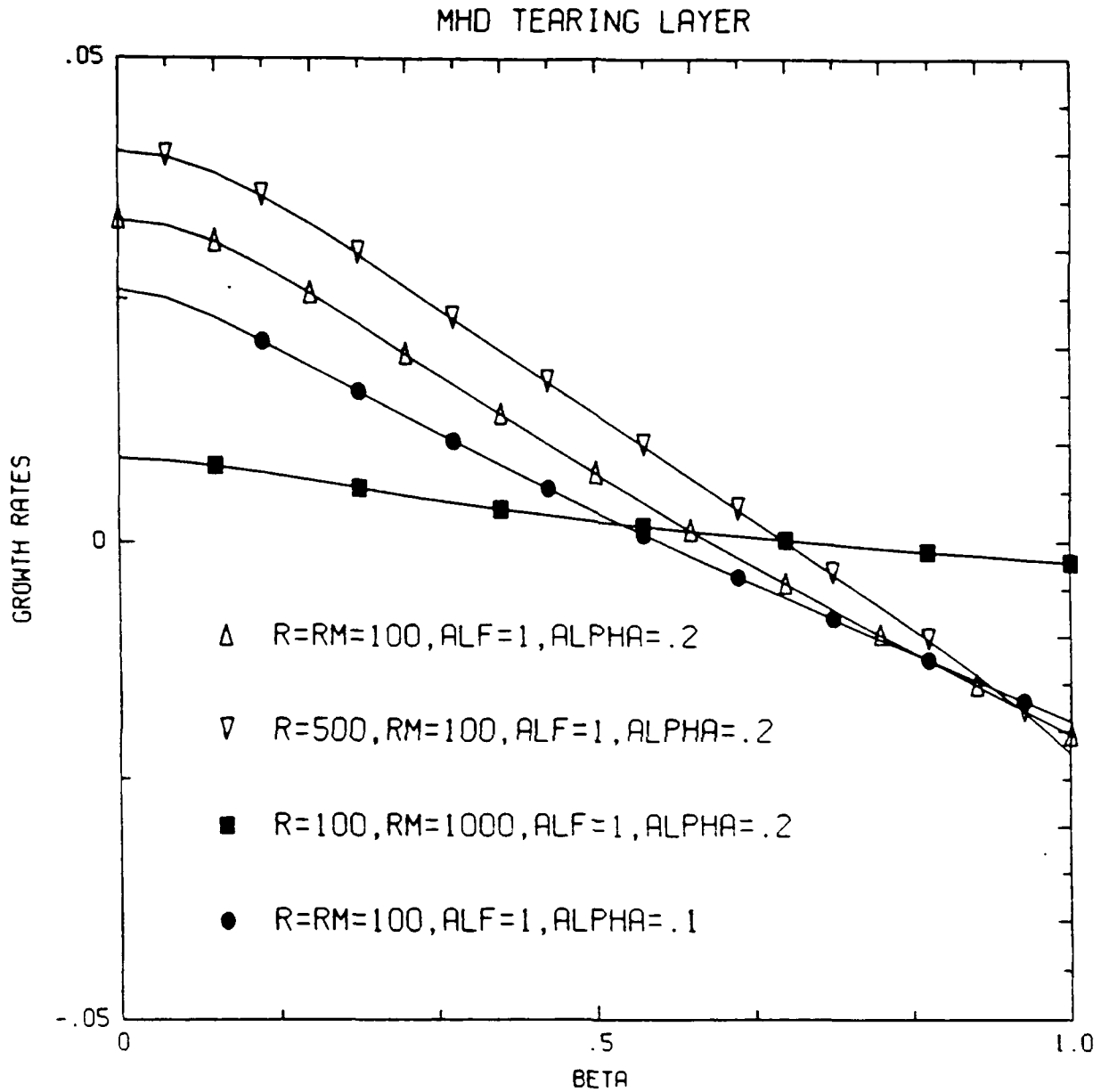


Figure 2. Growth rates of unstable eigenmode *vs* β , the sheetwise wavenumber. For the two-dimensional case, $\beta = 0$. The results confirm the Squires theorem.

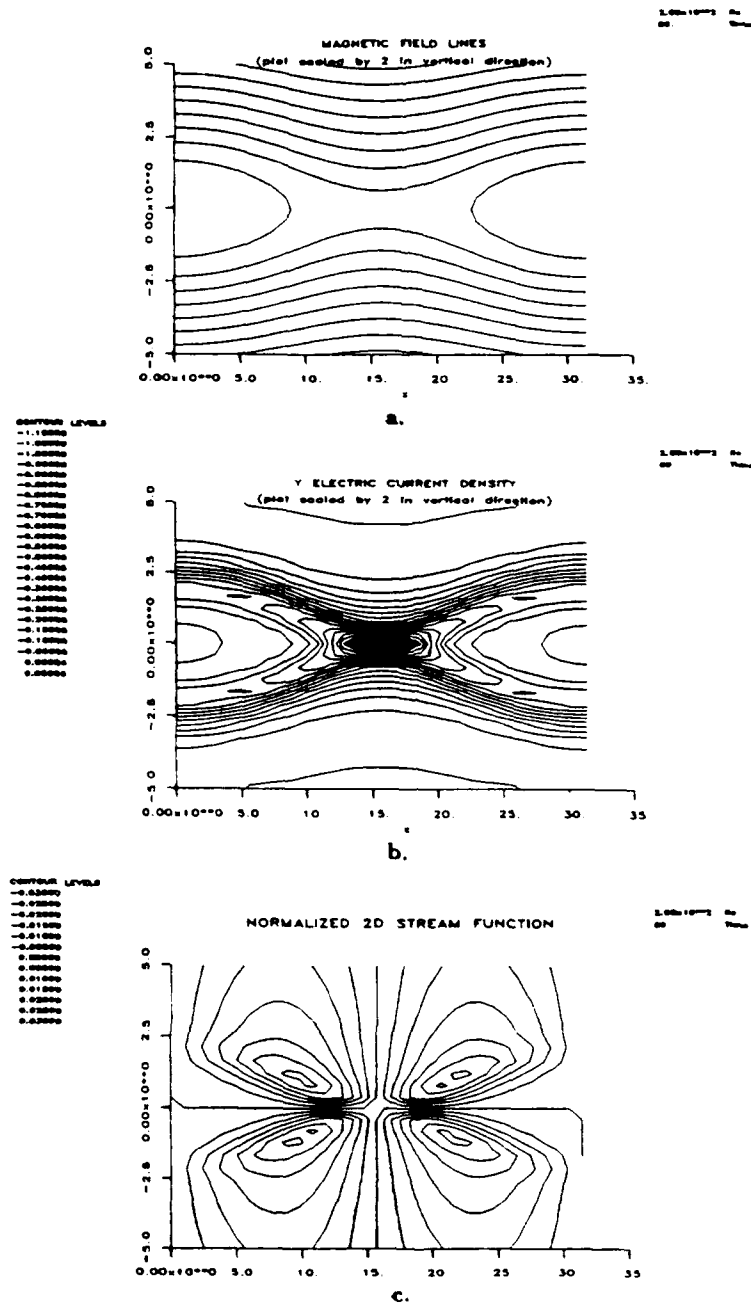


Figure 3. Contour plots in the $x - y$ plane exhibiting the structure of the 2D saturated state for case 9 of Table I: a. magnetic field, b. sheetwise electric current density and, c. velocity stream function.

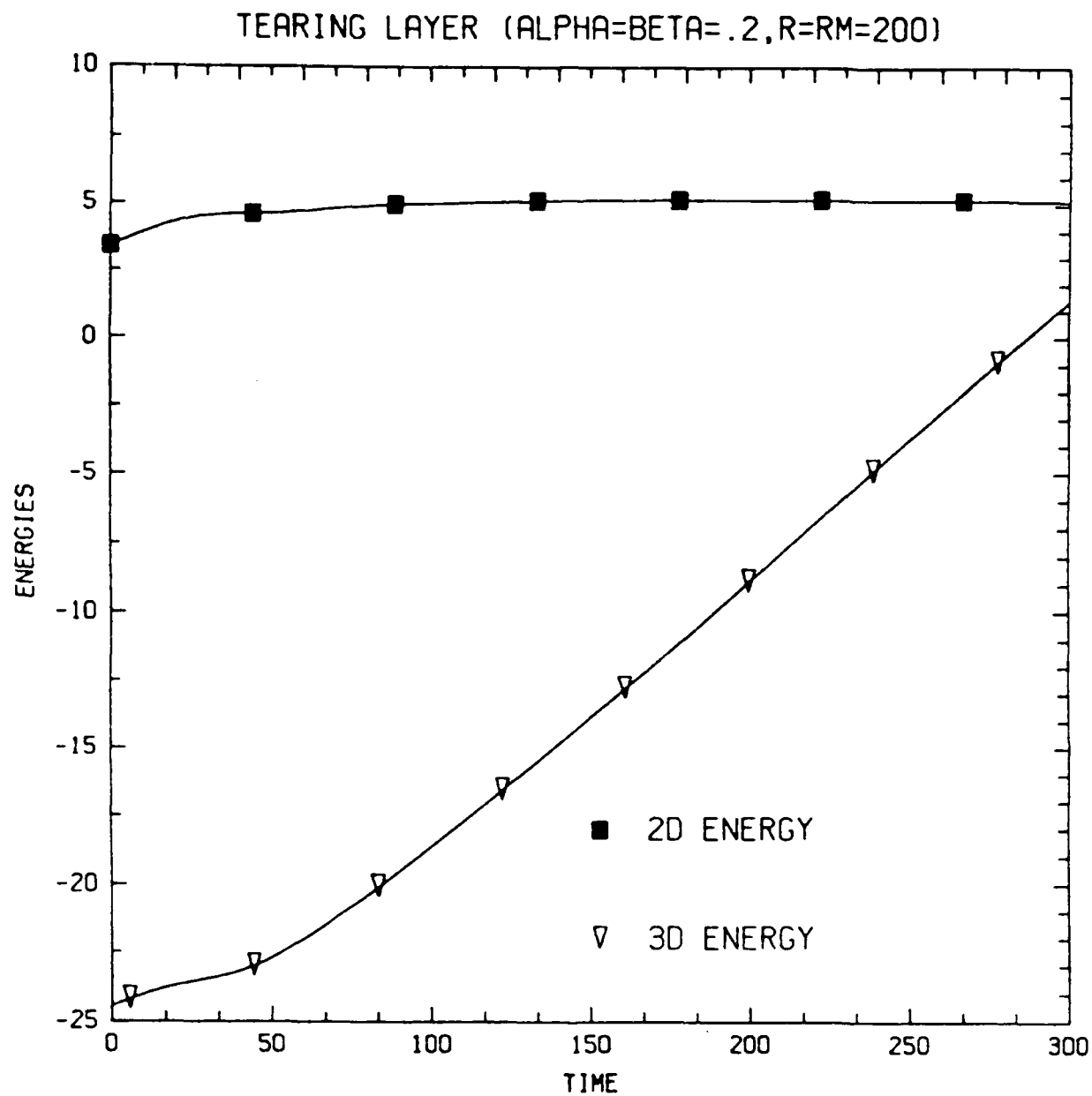


Figure 4. Time evolution of the logarithms of the two and three-dimensional total energies for case 9 in Table I. Note the existence of a well defined period of linear growth of the 3D modes after the 2D modes saturate.

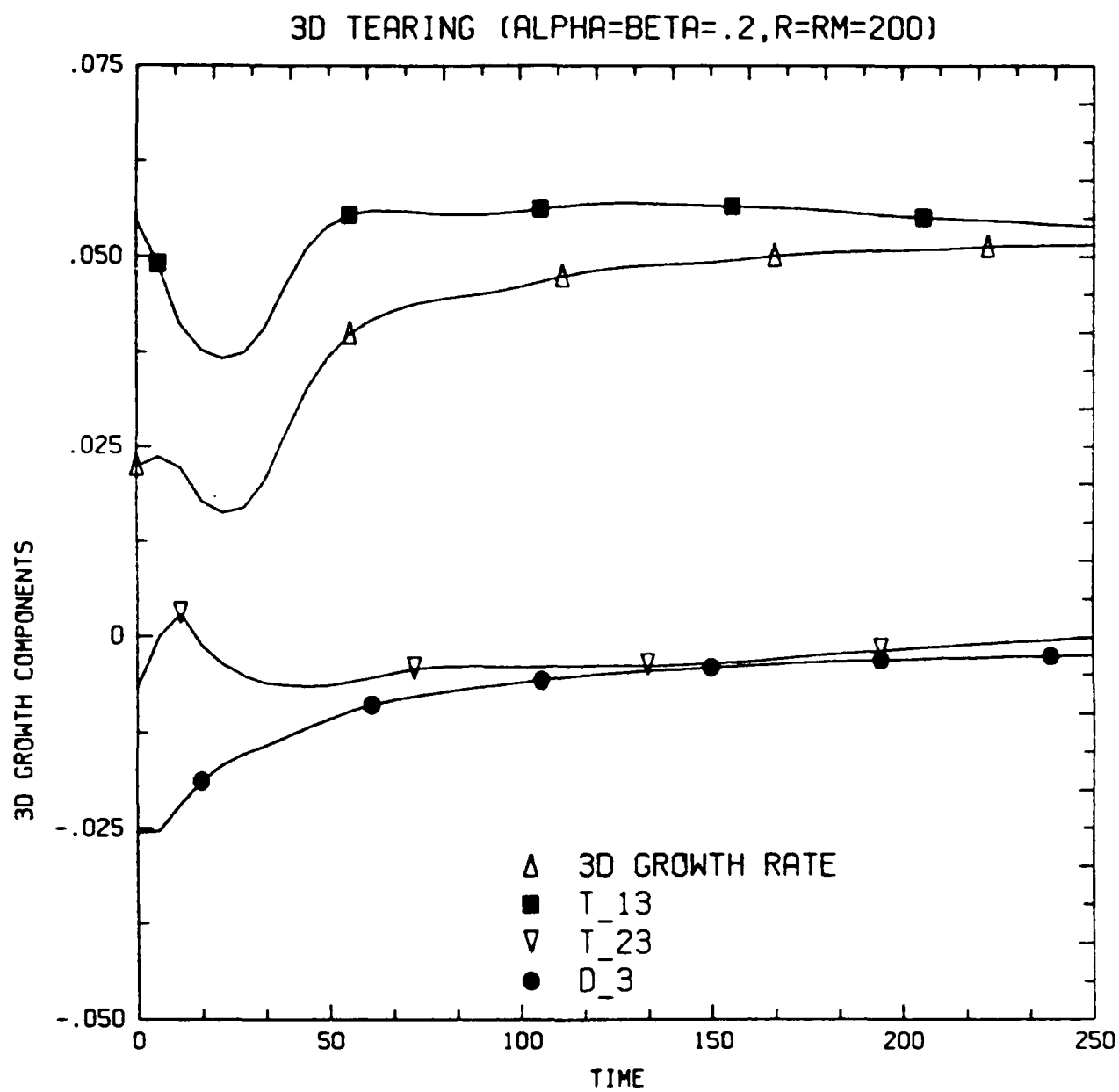


Figure 5. Time evolution of \bar{T}_{13} , \bar{T}_{23} , \bar{D}_3 and $\bar{\gamma}$ (3d growth rate) for case 9 of Table I.

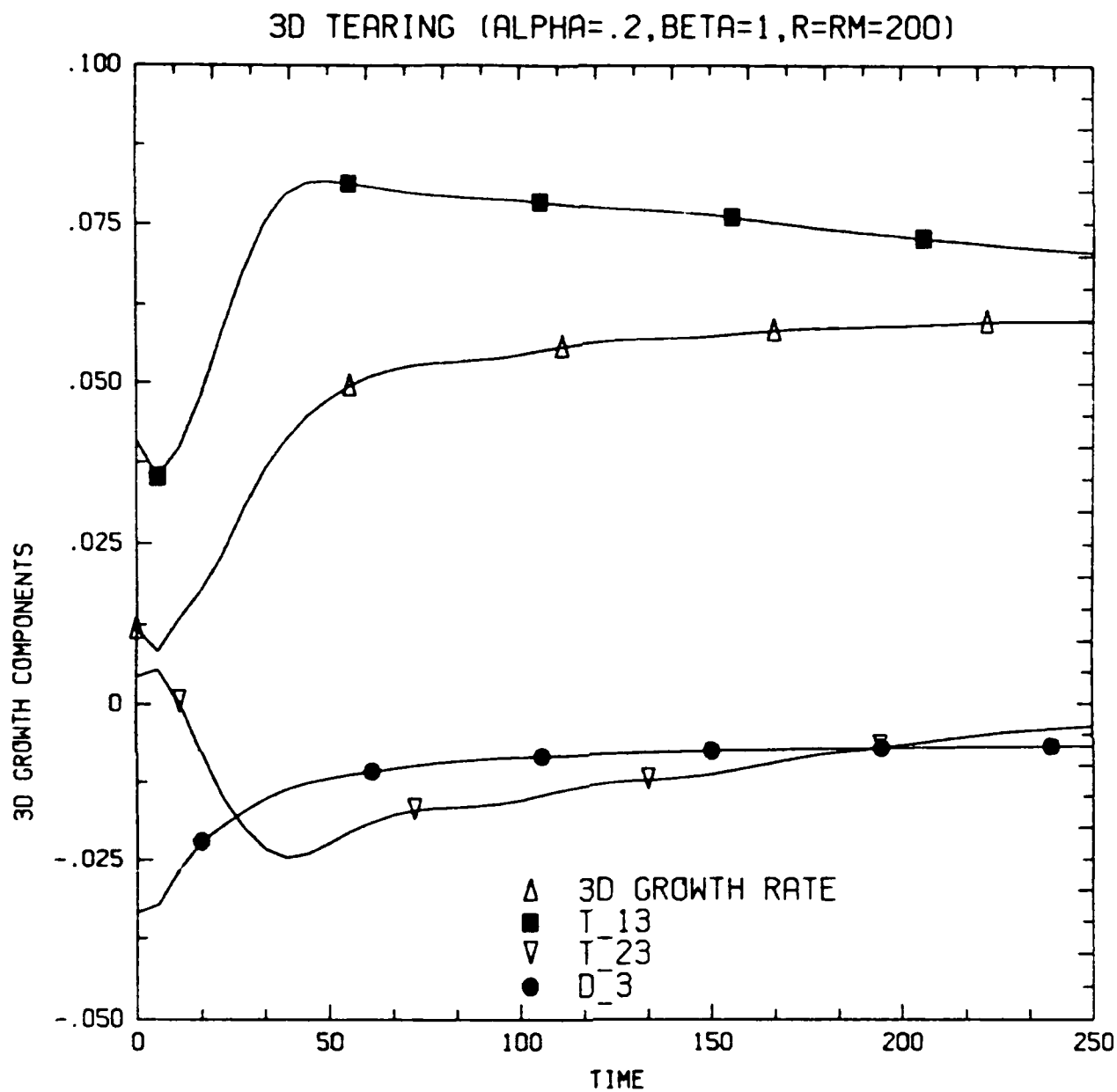


Figure 6. Time evolution of \bar{T}_{13} , \bar{T}_{23} , \bar{D}_3 and $\bar{\gamma}$ (3d growth rate) for case 11 of Table I.

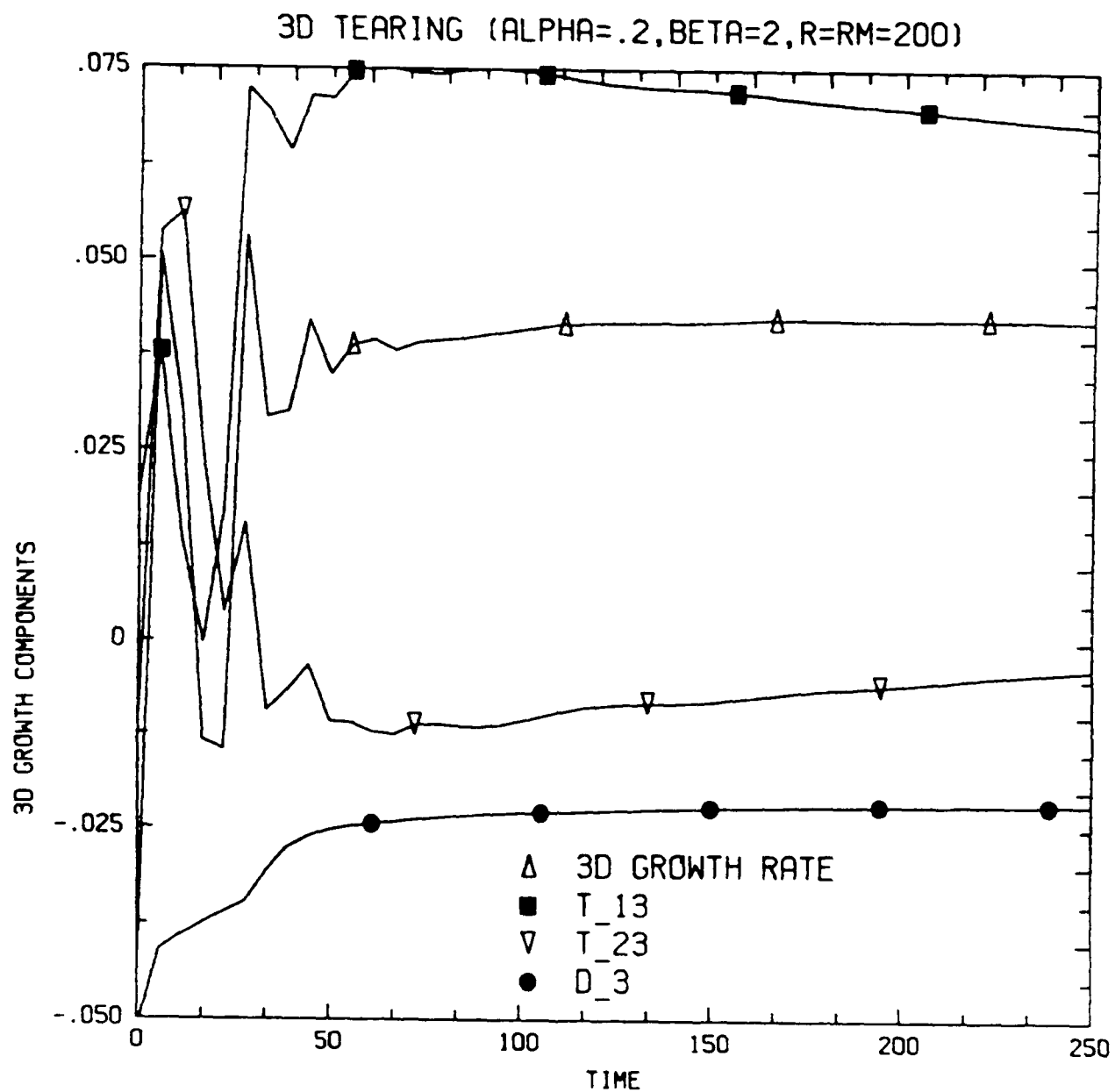


Figure 7. Time evolution of \bar{T}_{13} , \bar{T}_{23} , \bar{D}_3 and $\bar{\gamma}$ (3d growth rate) for case 13 of Table I.

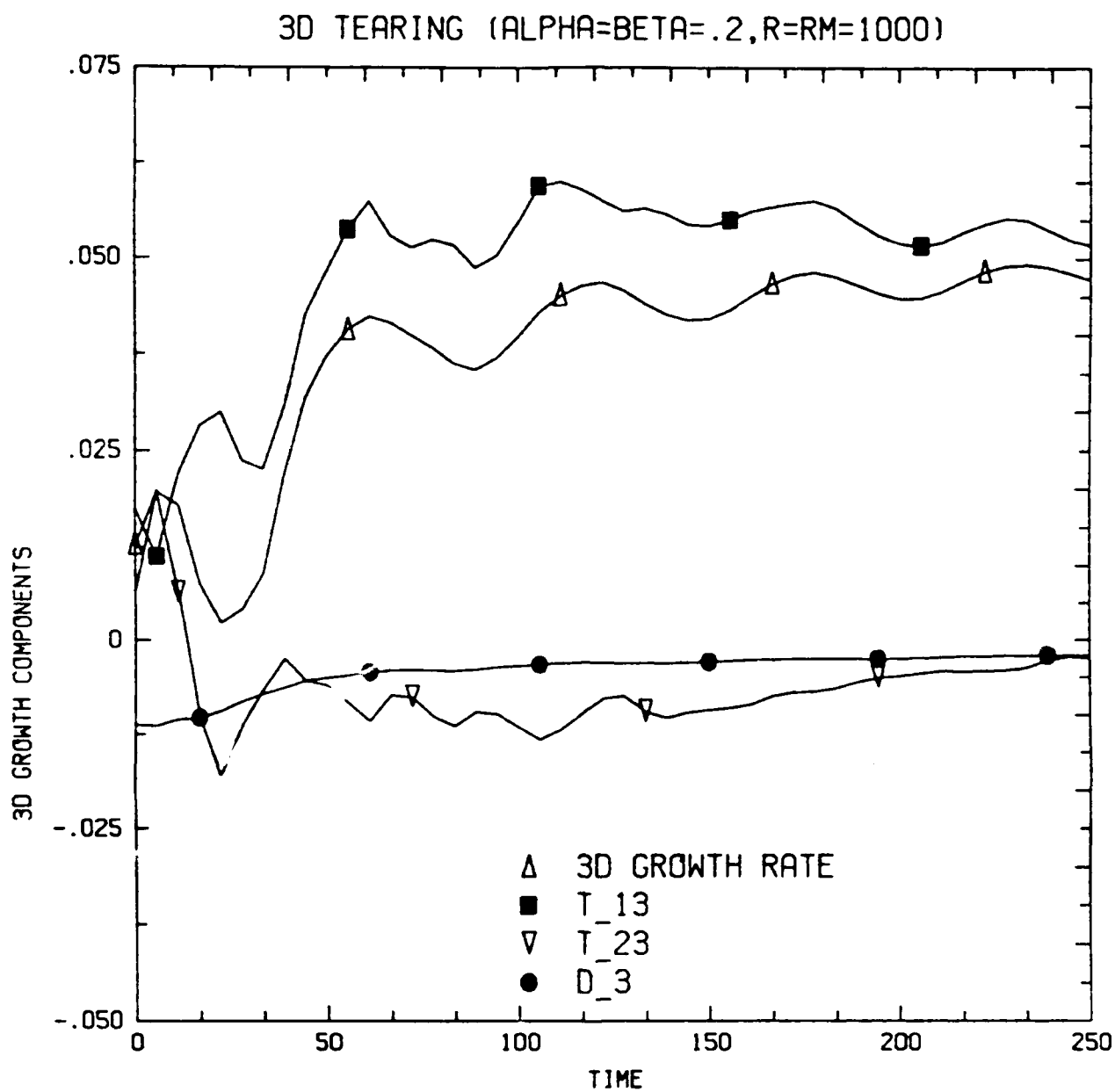


Figure 8. Time evolution of \bar{T}_{13} , \bar{T}_{23} , \bar{D}_3 and $\bar{\gamma}$ (3d growth rate) for case 18 of Table I.

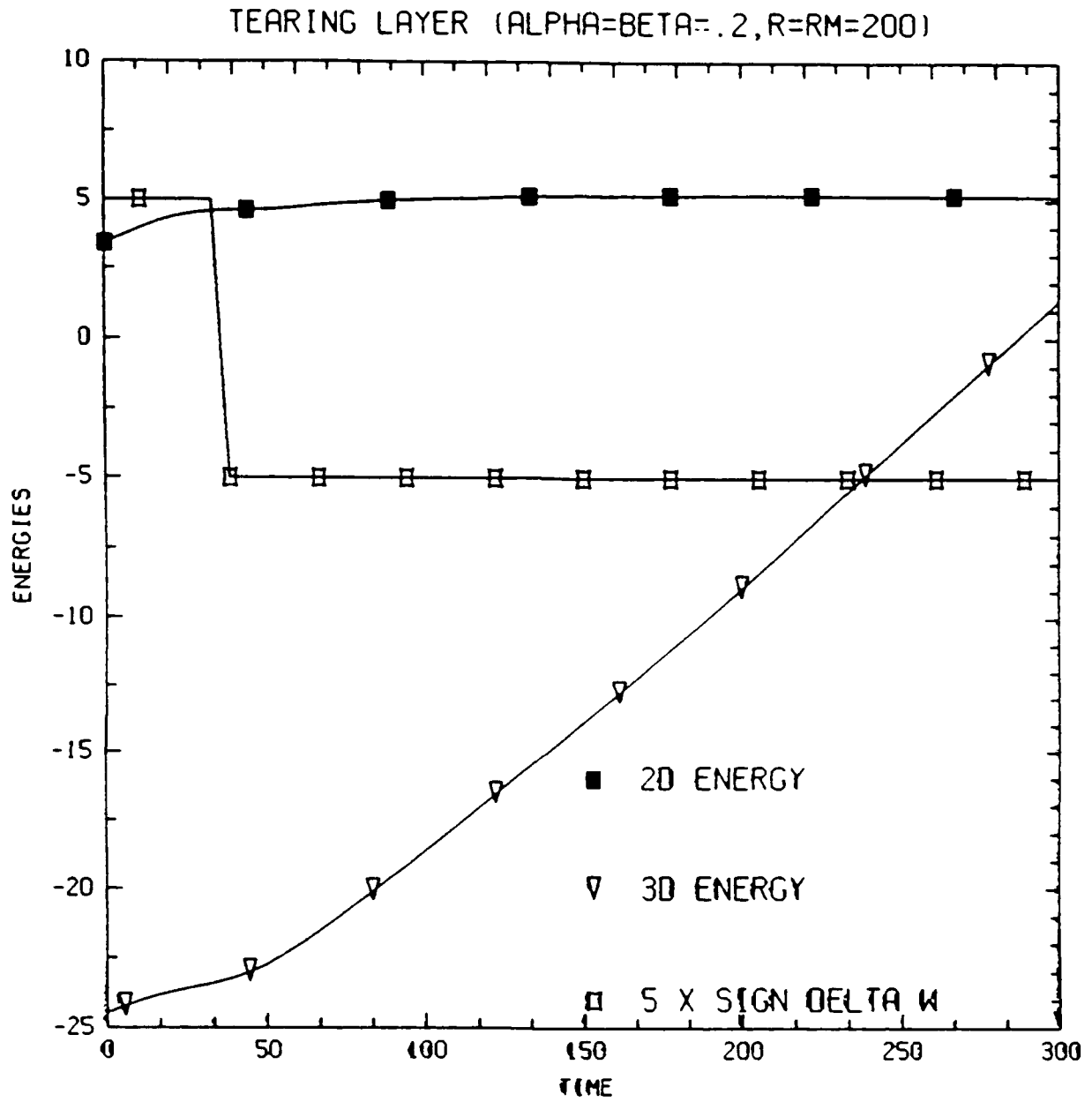


Figure 9. Time evolution of δW and the logarithms of the 2d and 3d total energies for case 9 of Table I.

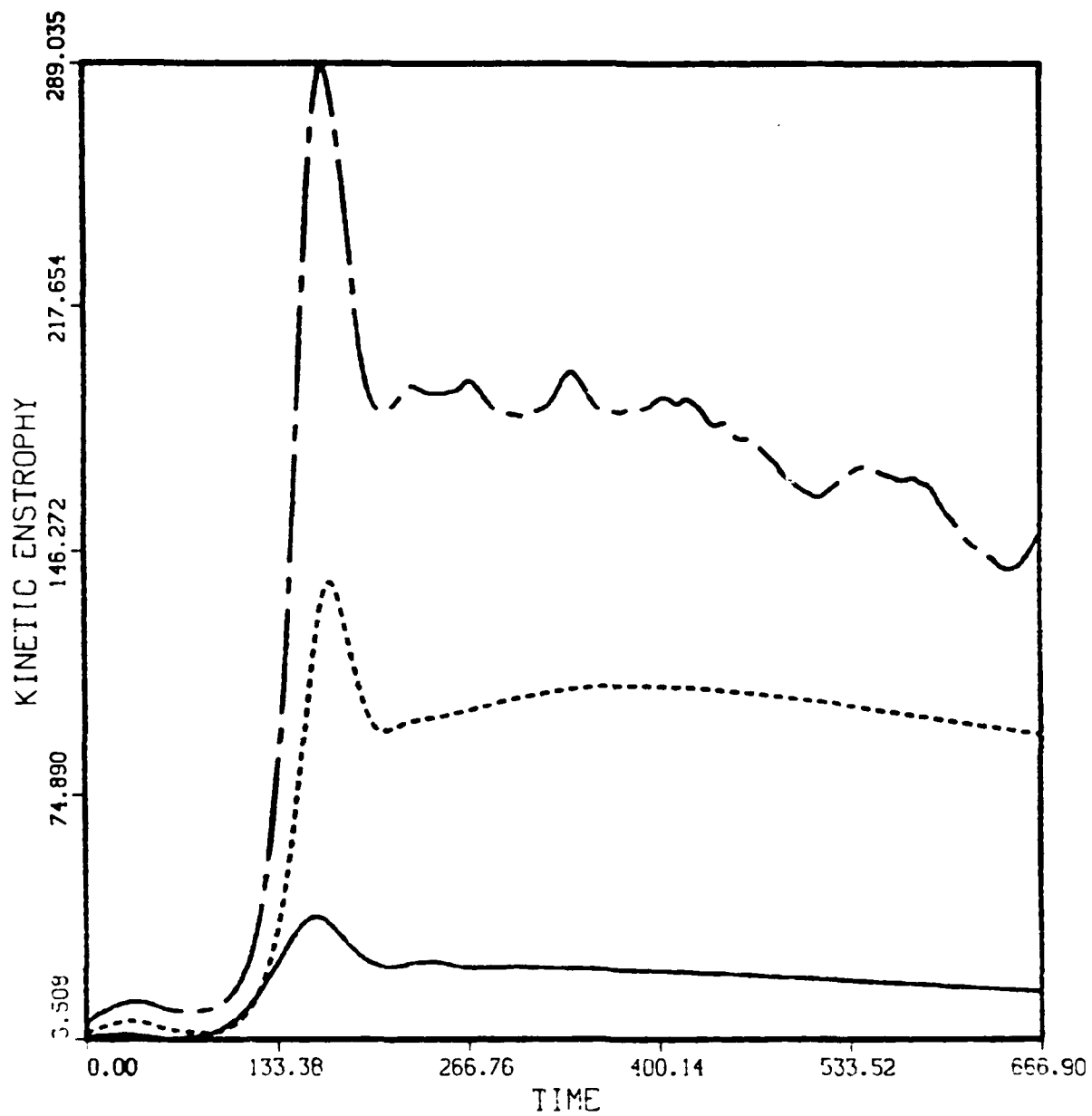


Figure 10. Time evolution of the enstrophies for cases 1, 2, and 3 of Table II. The solid line is case 1, the dashed line is case 2, and the mixed line is case 3.

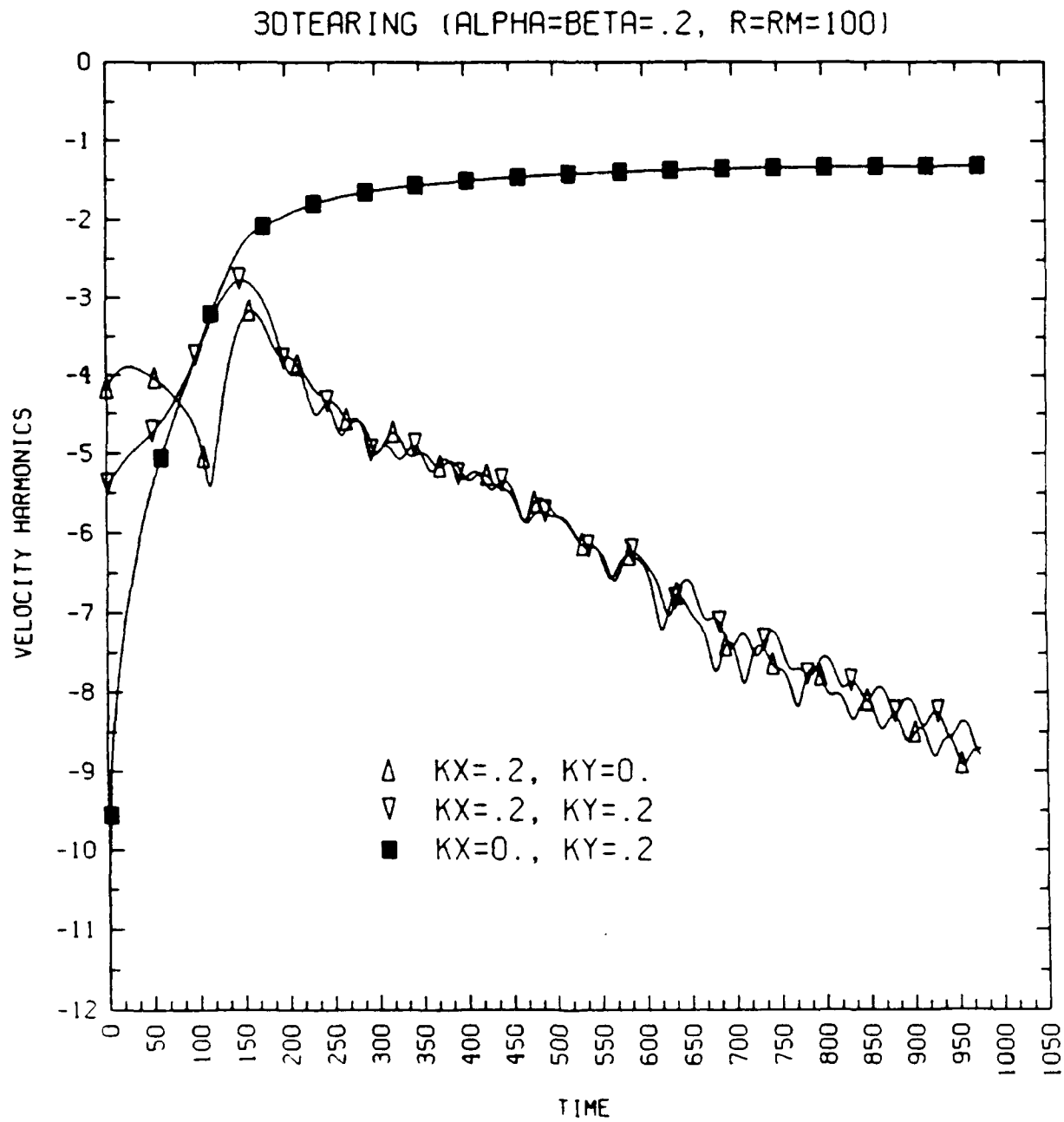


Figure 11. Time evolution of velocity modal energies: primary modes for case 2 of Table II.

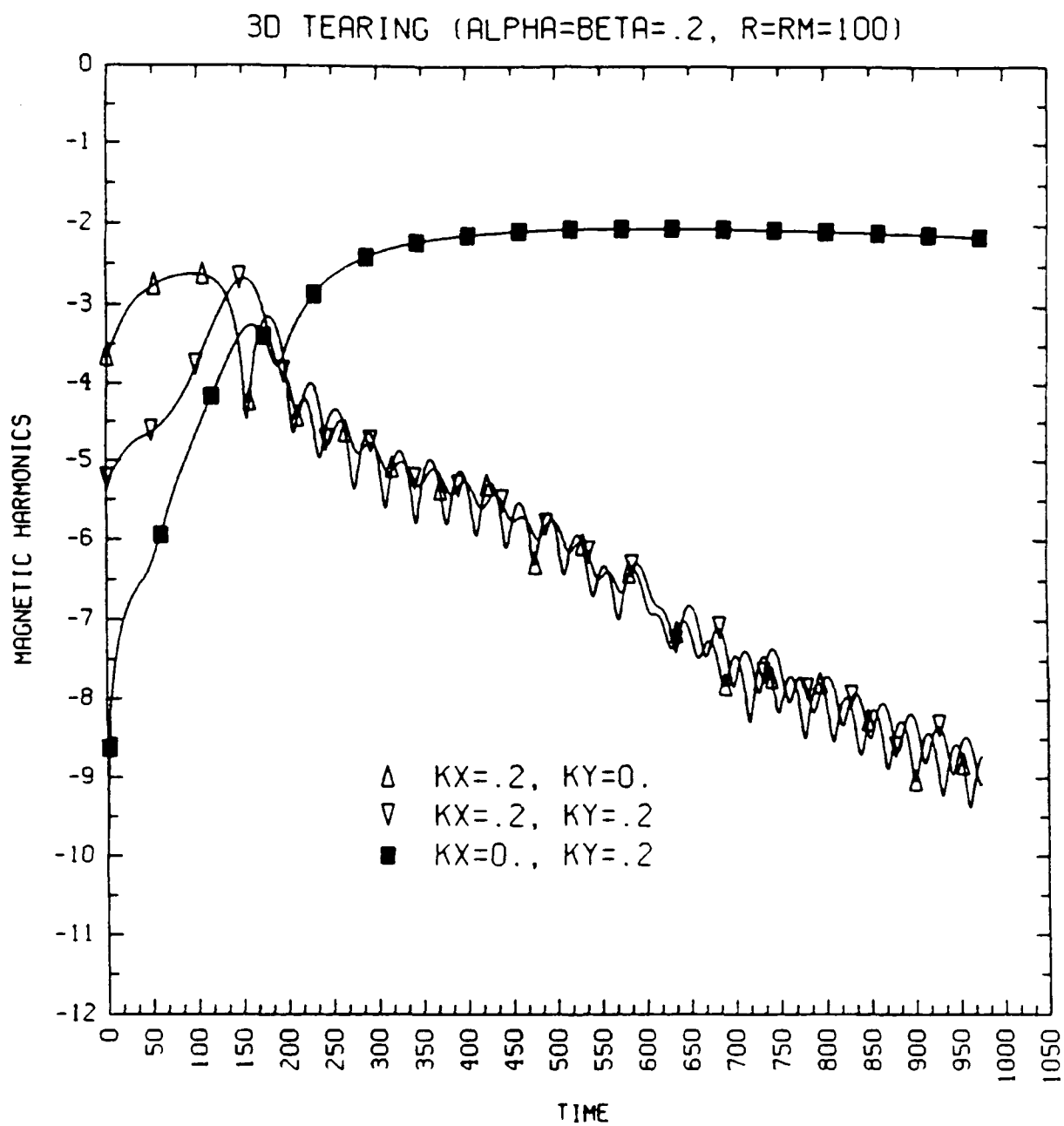


Figure 12. Time evolution of magnetic modal energies: primary modes for case 2 of Table II.

MAGNETIC FIELD MAGNITUDE ON NEUTRAL PLANE

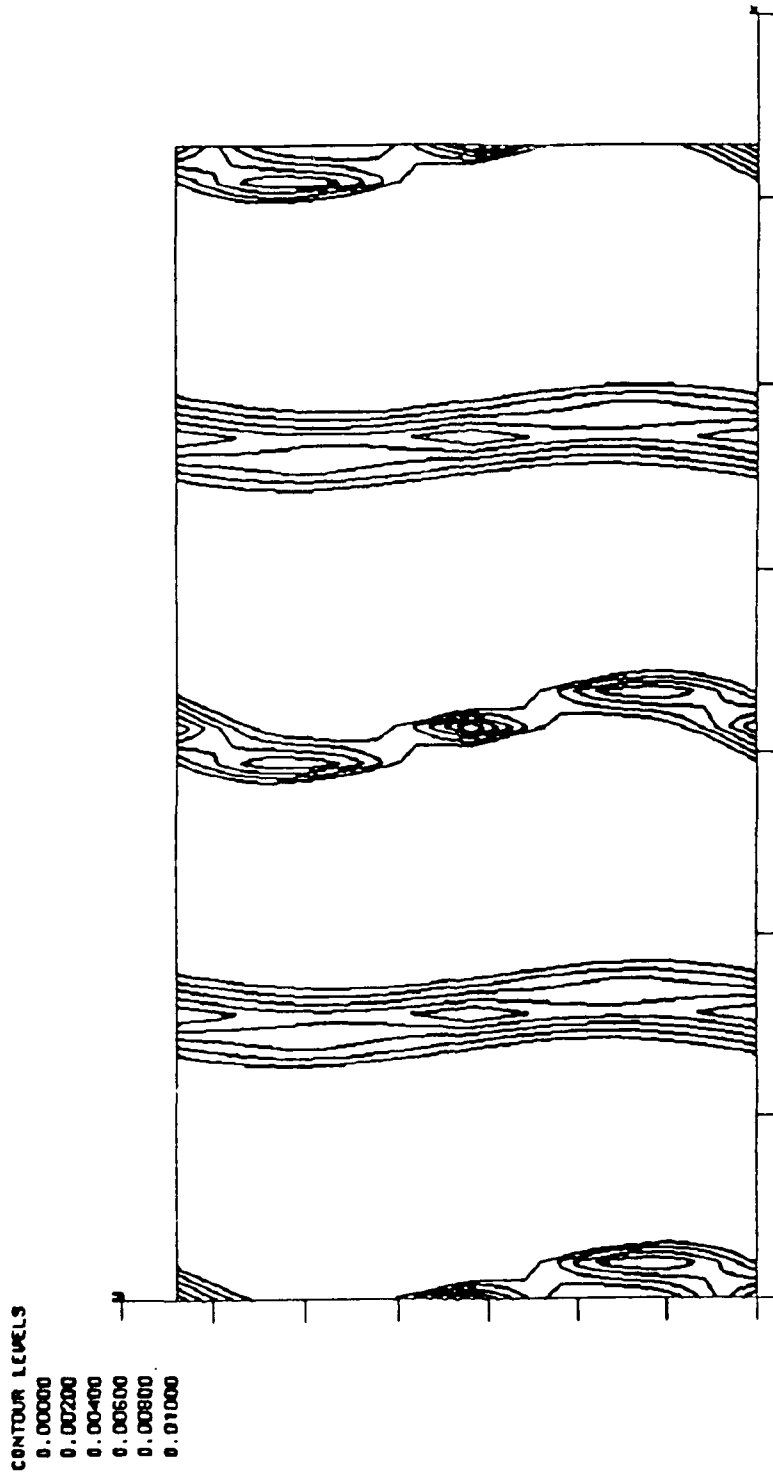


Figure 13. Contour plots of $|B|^2$ at $t = 44$ in the $(x, y, z = 0)$ plane for case 1 of Table II.
Two periods in x are shown.

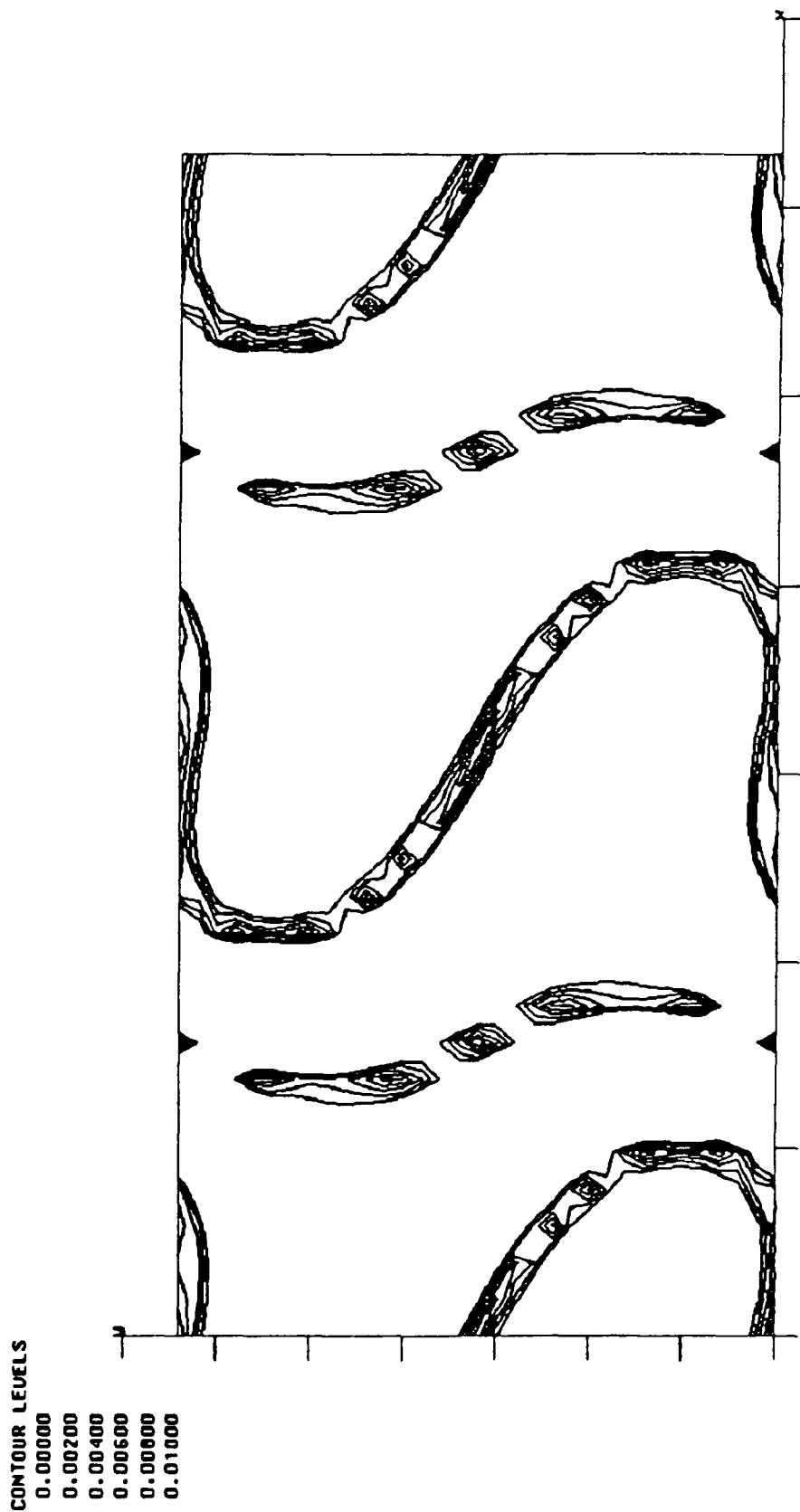


Figure 14. Contour plots of $|B|^2$ at $t = 133$ in the $(x, y, z = 0)$ plane for case 1 of Table II. Two periods in x are shown.

MAGNETIC FIELD MAGNITUDE ON NEUTRAL PLANE

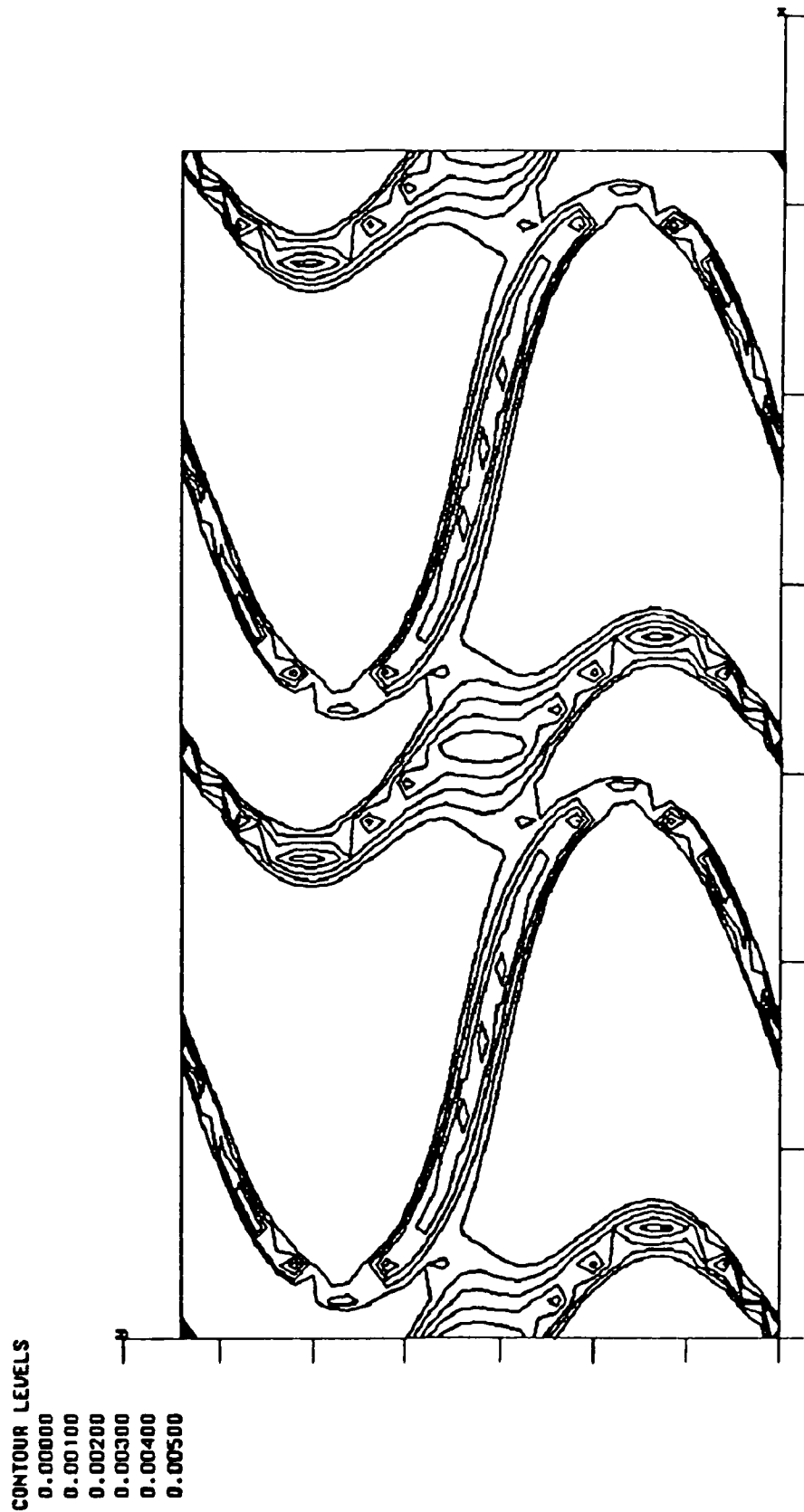


Figure 15. Contour plots of $|B|^2$ at $t = 222$ in the $(x, y, z = 0)$ plane for case 1 of Table

II. Two periods in x are shown.

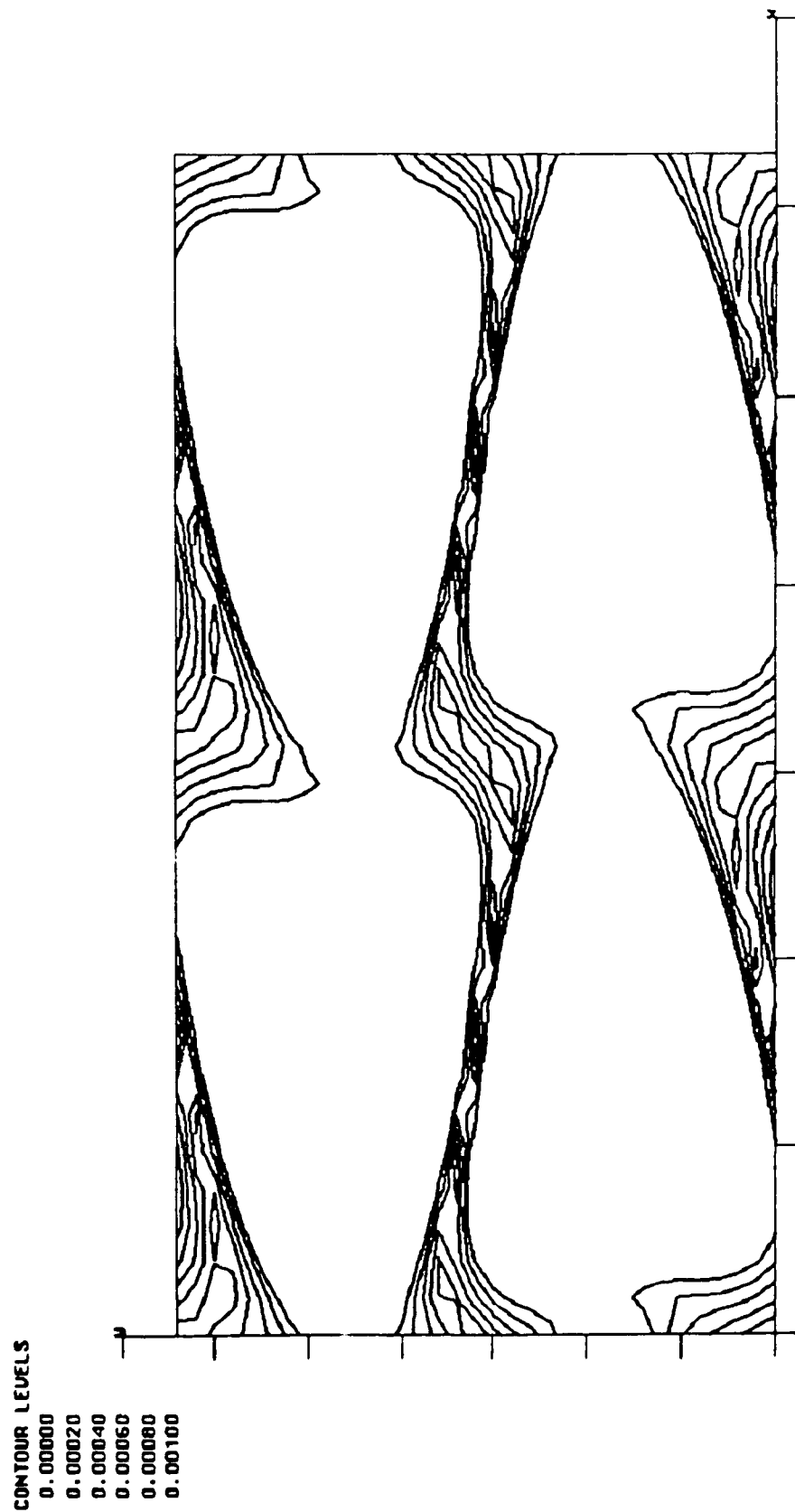


Figure 16. Contour plots of $|B|^2$ at $t = 444$ in the $(x, y, z = 0)$ plane for case 1 of Table II. Two periods in x are shown.

MAGNETIC FIELD MAGNITUDE ON NEUTRAL PLANE

CONTOUR LEVELS

0.00000
0.00020
0.00040
0.00060
0.00080
0.00100

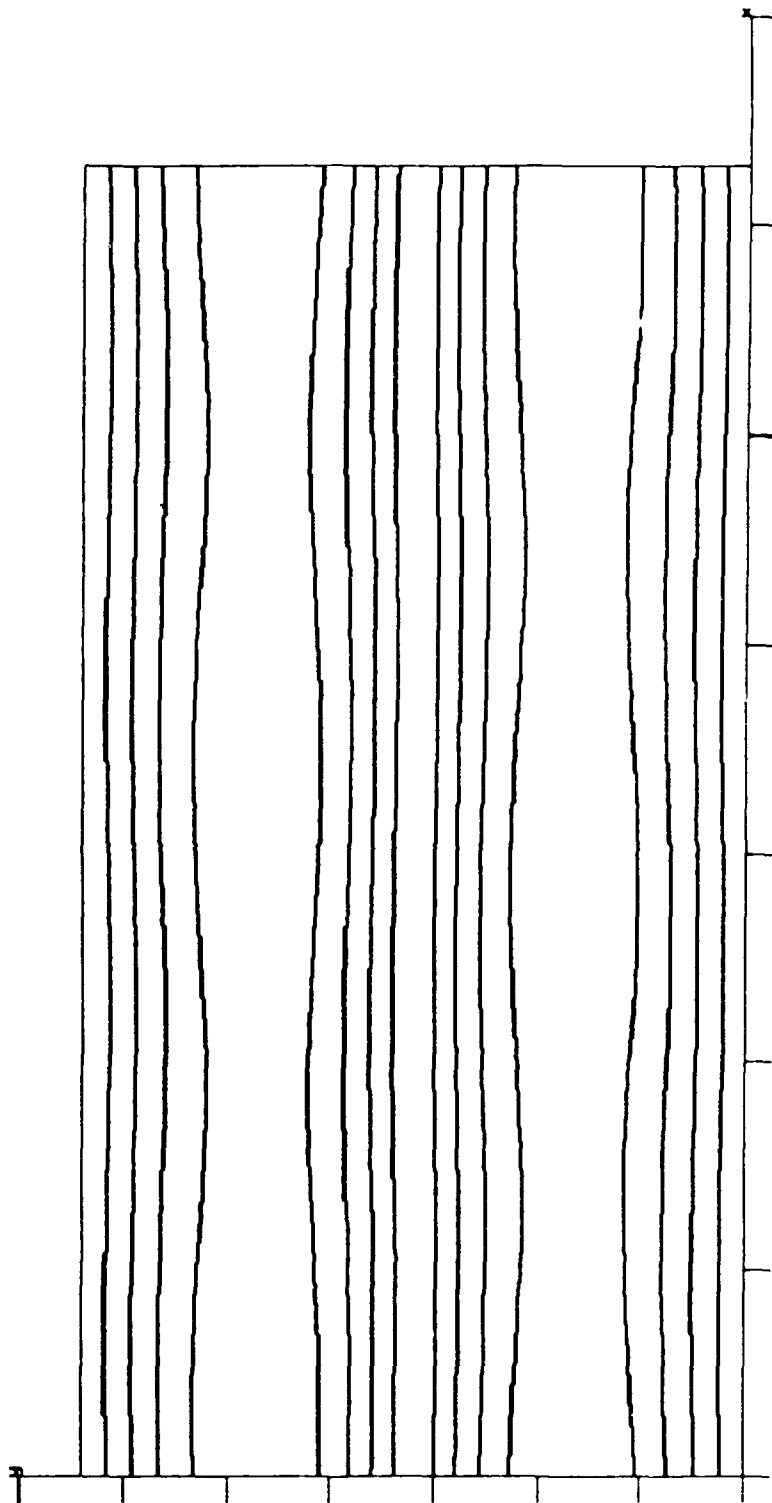


Figure 17. Contour plots of $|B|^2$ at $t = 1020$ in the $(x, y, z = 0)$ plane for case 1 of Table

II. Two periods in x are shown.